Article

Cell Stem Cell

Epithelial Sodium Channel Regulates Adult Neural Stem Cell Proliferation in a Flow-Dependent Manner

Graphical Abstract

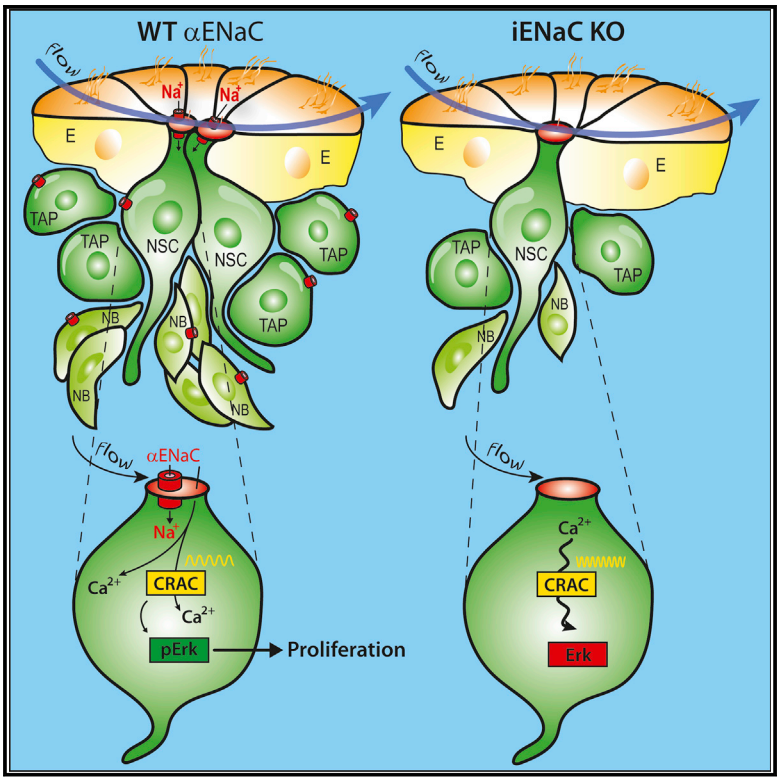

Authors

David Petrik, Michael H. Myoga, Sofia Grade, ..., Christine R. Rose, Benedikt Grothe, Magdalena Götz

Correspondence

magdalena.goetz@helmholtz-muenchen.de

In Brief

Stem cells need to adapt to signals from the environment to regulate their output. Here, we show the key role of a flow-sensitive ion channel in regulating the activation of adult neural stem cells and their output.

Highlights

- ENaC is high in adult NSCs and neuroblasts
- Knocking out ENaC in adult NSCs and neuroblasts decreases their proliferation
- Fluid flow promotes Na signals and changes Ca signals
- Fluid flow promotes proliferation in an ENaC-dependent manner

Petrik et al., 2018, Cell Stem Cell *22*, 865–878
June 1, 2018
https://doi.org/10.1016/j.stem.2018.04.016

CellPress

Cell Stem Cell
Article

Epithelial Sodium Channel Regulates Adult Neural Stem Cell Proliferation in a Flow-Dependent Manner

David Petrik,[1,2] Michael H. Myoga,[3,4] Sofia Grade,[1,2] Niklas J. Gerkau,[5] Melanie Pusch,[2] Christine R. Rose,[5,7] Benedikt Grothe,[3,4,6,7] and Magdalena Götz[1,2,6,7,8,*]

[1]Division of Physiological Genomics, Biomedical Center, Ludwig-Maximilians-Universitaet Munich, Planegg-Martinsried 82152, Germany
[2]Institute of Stem Cell Research, Helmholtz Center Munich, German Research Center for Environmental Health, Oberschleissheim 85764, Germany
[3]Division of Neurobiology, Ludwig-Maximilians-Universitaet Munich, Planegg-Martinsried 82152, Germany
[4]Max Planck Institute of Neurobiology, Planegg-Martinsried 82152, Germany
[5]Institute of Neurobiology, Faculty of Mathematics and Natural Sciences, Heinrich Heine University Duesseldorf, Duesseldorf 40225, Germany
[6]SYNERGY, Excellence Cluster of Systems Neurology, Biomedical Center, Ludwig-Maximilians-Universitaet, Munich, Germany
[7]Senior author
[8]Lead Contact
*Correspondence: magdalena.goetz@helmholtz-muenchen.de
https://doi.org/10.1016/j.stem.2018.04.016

SUMMARY

One hallmark of adult neurogenesis is its adaptability to environmental influences. Here, we uncovered the epithelial sodium channel (ENaC) as a key regulator of adult neurogenesis as its deletion in neural stem cells (NSCs) and their progeny in the murine subependymal zone (SEZ) strongly impairs their proliferation and neurogenic output in the olfactory bulb. Importantly, alteration of fluid flow promotes proliferation of SEZ cells in an ENaC-dependent manner, eliciting sodium and calcium signals that regulate proliferation via calcium-release-activated channels and phosphorylation of ERK. Flow-induced calcium signals are restricted to NSCs in contact with the ventricular fluid, thereby providing a highly specific mechanism to regulate NSC behavior at this special interface with the cerebrospinal fluid. Thus, ENaC plays a central role in regulating adult neurogenesis, and among multiple modes of ENaC function, flow-induced changes in sodium signals are critical for NSC biology.

INTRODUCTION

Since the discovery of adult neurogenesis in birds and mammals, its regulation by various environmental signals has been a subject of keen interest (Lim and Alvarez-Buylla, 2016). However, adult NSCs in the mammalian brain are located in different niches. In the subependymal zone (SEZ), neural stem cells (NSCs) are embedded in a layer of ependymal cells with their apical ends projecting into the ventricular space filled with cerebrospinal fluid (CSF) (Doetsch et al., 1997; Mirzadeh et al., 2008; Ninkovic and Götz, 2015; Silva-Vargas et al., 2016). This cytoarchitecture places NSCs at the intersection between brain parenchyma and CSF allowing them to sense changes in both and then propagate this information in the syncytium (Lim and Alvarez-Buylla, 2016). Some key elements, such as neuroendocrine peptides and trophic factors (Lehtinen et al., 2011; Silva-Vargas et al., 2016), were identified in the CSF to regulate NSCs biology. Similarly, a gradient of CSF chemorepulsive factors was found to direct migration of neuroblasts (Sawamoto et al., 2006). However, the molecular sensors detecting the CSF flow remain so far unknown.

Ion channels are prime candidates for such sensor as they can merge different stimuli into a simple and fast signal, the change in flow of ions down the electrochemical gradient and across the plasma membrane. However, NSCs share most electrophysiological properties with astrocytes (Fukuda et al., 2003; Liu et al., 2006), including expression of common voltage-gated potassium channels (Butt and Kalsi, 2006; Prüss et al., 2011). To determine differences in ion channel expression between these cell types, we searched in our previous genome-wide expression analysis and identified the epithelium sodium channel (ENaC) as having higher expression in NSCs compared to parenchymal astrocytes in the diencephalon or cerebral cortex (Beckervordersandforth et al., 2010; Sirko et al., 2015).

ENaC is often located on the apical membrane (Enuka et al., 2012) and controls transepithelial flux of sodium in kidneys or lungs (Hanukoglu and Hanukoglu, 2016), where it is found also in stem cells (Liu et al., 2016). In the nervous system, it is expressed in brain centers controlling fluid volume or blood pressure (Amin et al., 2005), in retina, olfactory bulb (OB) and human cortex (Dyka et al., 2005; Giraldez et al., 2007), in choroid plexus (Van Huysse et al., 2012) and mechanosensory neurons (Fricke et al., 2000). Among glial cells, ENaC has been described in retinal Müller glia (Brockway et al., 2002) and certain glioma cells (Miller and Loewy, 2013).

ENaC is different from other voltage- or ligand-gated channels as it is generally open and hence provides a constant sodium (Na) influx. However, its conductance properties and/or opening probability are regulated by many mechanisms including second messengers, proteases, and post-translation modifications (Boscardin et al., 2016). Because ENaC is sensitive also to fluid shear stress (Fronius et al., 2010; Wang et al., 2009), it may represent

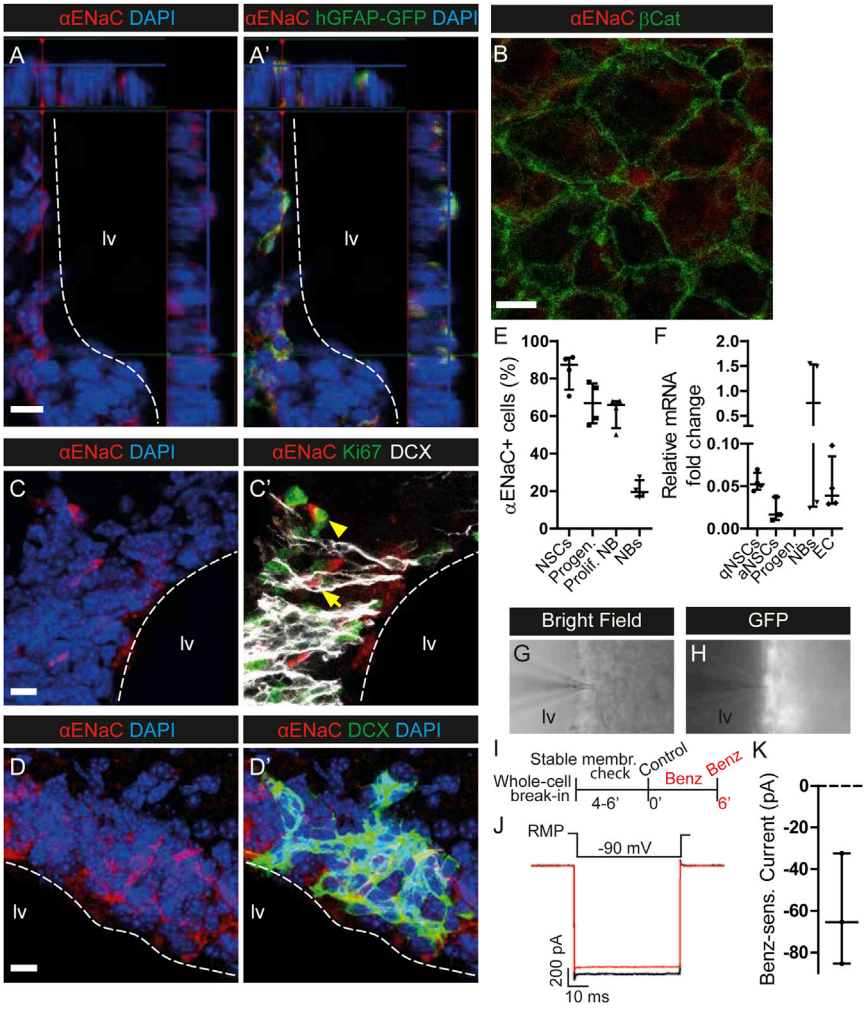

Figure 1. ENaC Expression in Subependymal Zone

(A) Confocal microphotograph of immunostaining for αENaC and hGFAP-GFP in SEZ (lv, lateral ventricle).

(B) αENaC staining in β-catenin pinwheel structures of SEZ whole mounts.

(C) Ki67-positive (Ki67$^+$, arrowhead) and Ki67$^+$ DCX$^+$ (arrow) cells in SEZ express αENaC.

(D) In SEZ, αENaC overlaps with DCX$^+$ cells.

(E) Proportional analysis of adult neural stem cells (NSCs), progenitors (Progen.), proliferating neuroblasts (Prolif. NBs), and NBs in SEZ that are αENaC$^+$.

(F) Relative mRNA fold change of αENaC when compared to GAPDH in cDNA from sorted quiescent NSCs (qNSCs; hGFAP-GFP$^+$, CD133$^+$), activated NSCs (aNSCs, hGFAP-GFP$^+$, CD133$^+$, EGFR$^+$), Progen. (hGFAP-GFP$^-$, CD133$^-$, EGFR$^+$), NBs (PSA$^-$NCAM$^+$), and ependymocytes (EC; hGFAP$^-$GFP$^-$, Prominin$^+$).

(G and H) Microphotographs in bright-field (G) and fluorescence (H) showing a patch-clamp electrode on a GFP$^+$ cell on the very edge of SEZ.

(I) Patch-clamp experimental paradigm.

(J) Voltage-command and an example of whole-cell currents elicited by a −90-mV rectangular pulse (40 ms long) before (black) and 6 min after Benzamil perfusion (red).

(K) Benz-sensitive currents at −90 mV.

Scale bars, all 10 μm. Animals were tested at 6–8 weeks of age. n = 4 for proportional analysis, n = 10 for each of 4 FACS experiments, n = 3 for patch-clamp recordings. Data are presented as median ± interquartile range (IQR).

a bona fide candidate for the elusive molecular sensor detecting CSF flow and linking NSCs with activity of the ciliated ependymal cells that surround them in the SEZ (Mirzadeh et al., 2008).

RESULTS

αENaC Is Expressed in NSCs and Progenitors in the SEZ

To determine the localization of ENaC in the SEZ of adult mice, we immunostained for the pore-forming alpha subunit of ENaC (αENaC) with cell-type-specific antibodies (Figure 1) and observed αENaC in NSCs labeled by the expression of the green fluorescent protein (GFP) driven by the promoter of human glial fibrillary acidic protein (GFAP, Figure 1A) or nestin ((Yamaguchi et al., 2000) Figure S1A) or GFAP and Sox2 immunoreactivity (López-Juarez et al., 2012; Figure S1B). Indeed, αENaC staining was also present in the NSCs located in the core of the pinwheel structures (Figures 1B and S1C) labeled by β-catenin and hGFAP-GFP (Beckervordersandforth et al., 2010; Mirzadeh et al., 2008). Also proliferating cells labeled with Ki67 (Scholzen and Gerdes, 2000) and Doublecortin (DCX)$^+$ neuroblasts (Gleeson et al., 1999) were αENaC immunopositive. Interestingly, this was the case only in the SEZ (Figures 1C and 1D), and not in the rostral migratory stream (RMS, Figure S1D). Taken together, αENaC was detectable in over 80% of NSCs including proliferating Ki67$^+$GFAP$^+$ NSCs (Figures S1E and S1F). Also 60% of progenitors and a subset of about 20% neuroblasts (Figure 1E) in the SEZ had detectable levels of αENaC protein. In contrast, niche cells were immunonegative (Figure S1G for oligodendrocyte progenitors, Figure S1H for niche astrocytes), except weak staining in ependymal cells (Figure 1B).

The hippocampal subgranular zone (SGZ) showed more restricted αENaC-immunostaining with rare GFAP$^+$, nestin-GFP$^+$ or Sox2$^+$ NSCs, and some DCX$^+$ neuroblasts (Figures S1I–S1K), while parenchymal astrocytes were ENaC negative (Figure S1L).

We also checked mRNA levels of α, β, and γENaC subunits from dissected SEZ by qRT-PCR and found αENaC expressed much higher than β or γENaC (Figure S1M). The comparison of relative mRNA expression ($2^{-\Delta\Delta Ct}$; (Livak and Schmittgen, 2001) revealed 15 times more αENaC in the SEZ than in the OB, but about 9 times less compared to kidney. When SEZ cells were isolated by fluorescence-activated cell sorting (FACS) as previously described (Codega et al., 2014; Fischer et al., 2011), αENaC but not β or γ expression was detected in quiescent and activated NSCs and ependymal cells (Figure 1F). Neuroblasts had higher variability of αENaC mRNA levels, while virtually nothing was detectable in transiently amplifying progenitors (TAPs) despite the presence of the ENaC protein in these cells (Figures 1C and 1E). This suggests either fast downregulation of ENaC mRNA

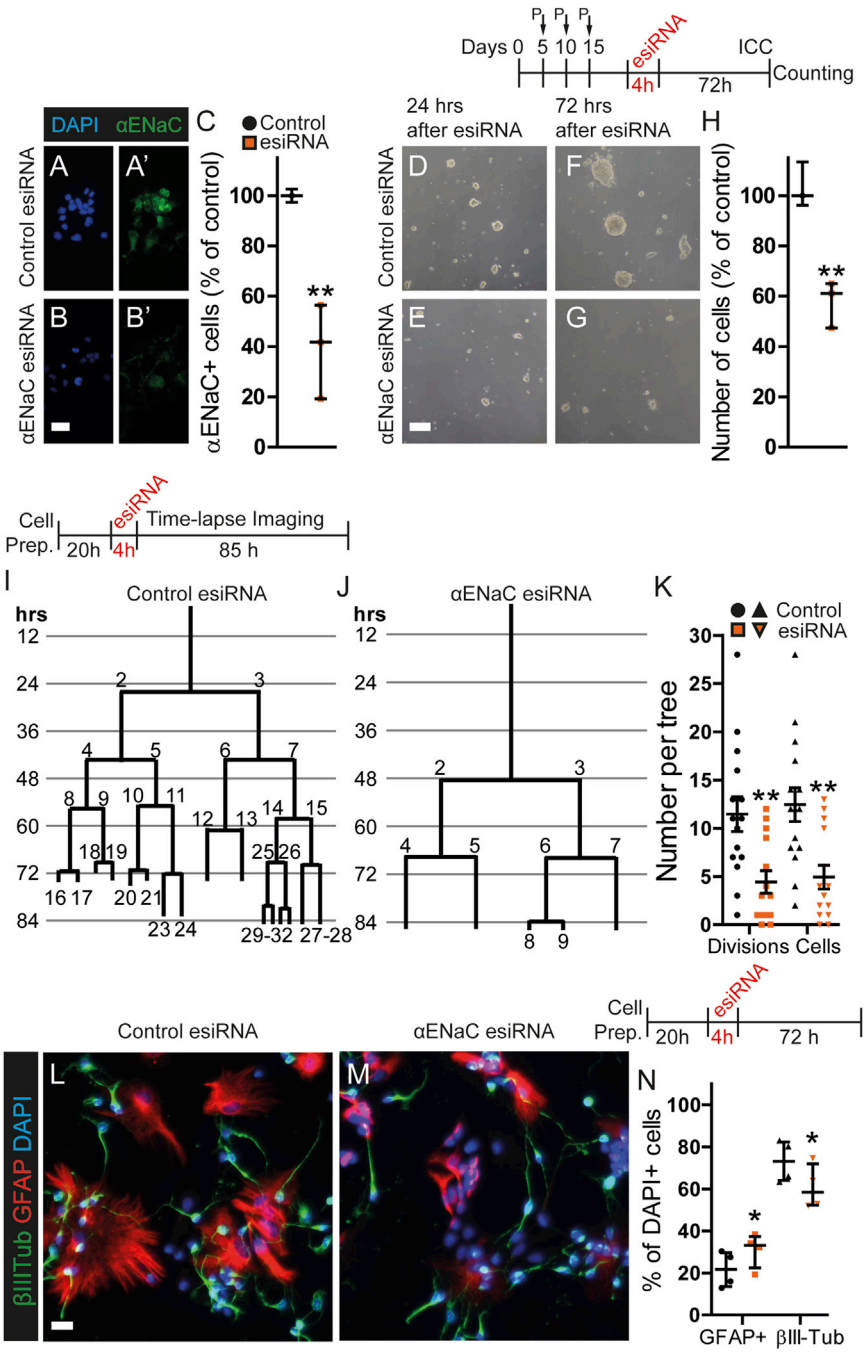

Figure 2. Reduced Proliferation and Survival upon Knocking Down of ENaC in Primary SEZ or Neurosphere-Derived Cells

(A and B) Immunostaining for αENaC and DAPI in primary SEZ cultures 48 hr after transfection with control esiRNA (A) or αENaC esiRNA (B).

(C) Proportion of primary SEZ cells immunopositive for αENaC normalized to control.

(D–G) Representative images of neurospheres after transfection with control esiRNA (D and F) or αENaC esiRNA (E and G) at two time points.

(H) Schematics of experimental paradigm and dissociated neurosphere cell number quantification 72 hr after esiRNA knockdown (KD) of αENaC normalized to control.

(I–K) Example cell division trees from time-lapse imaging in control (I) or αENaC esiRNA (J) during 85 hr after transfection. Quantification of the number of cell divisions and cells per division tree in αENaC KD (K).

(L and M) Representative images of primary SEZ cells grown in differentiating conditions stained as indicated after transfection with control (L) or αENaC (M) esiRNA.

(N) Quantification of proportion of cells positive for GFAP or βIII-tubulin.

Scale bars, 100 μm in (D)–(G) and 20 μm in (A), (B), (L), and (M). Animals were tested at 6–8 weeks of age. n = 3 for cell cultures. n = 12–16 for lineage trees. *p < 0.05; **p < 0.01. Data are presented as median ± IQR or given the normal distribution, as mean ± SEM (K).

upon dissociation or a high protein stability and inheritance of protein from NSCs in these cells. In order to test whether αENaC forms a functional channel in the SEZ, we performed whole-cell patch-clamp recordings and successfully isolated currents sensitive to the ENaC-specific blocker Benzamil (Alvarez de la Rosa et al., 2013) (Figures 1I–1K) in NSCs identified by Aldh1l1-GFP^{+} (Heintz, 2004) and a radial morphology (Figures 1G, 1H, and S1N).

ENaC Is Critical for SEZ Cell Proliferation *In Vitro*

To investigate the functional role of ENaC, we examined neurospheres from adult SEZ (of which 77% cells express αENaC, Figures S2A and S2B) subjected to genetic knockdown (KD) by esiRNA against αENaC or to pharmacological inhibition by ENaC-specific blockers Benzamil or Amiloride (Alvarez de la Rosa et al., 2013). In proliferating conditions, the αENaC KD, which shows about 60% reduction in ENaC-immunopositive cells (Figures 2A–2C), resulted in significantly fewer cells at 72 hr after transfection (Figures 2D–2H). Similarly, incubation of the neurospheres in Amiloride (Figure S2C) or Benzamil (Figures S2D–S2H) for 24 hr significantly reduced the number of cells in a concentration-dependent manner at 72 hr after the block. To determine whether this reduction in cell number is due to reduced proliferation and/or increased cell death, we followed single cells and their progeny for 85 hr by time-lapse imaging of primary SEZ cells as previously described (Ortega et al., 2011). Both αENaC KD (Figures 2I–2K) and Benzamil incubation (Figure S2I) significantly decreased the number of divisions and cells generated per individual cell lineage when compared to controls. Moreover, bath application of Benzamil-induced rapid cell death (average time 14.2 ± 1.6 hr) in about 60% compared to only 6% in control (Figures S2J–S2L). Thus, reducing function or protein levels of αENaC impairs proliferation and survival of primary SEZ cells.

Similarly, SEZ neurosphere-derived cells died as indicated by an increase in TUNEL$^+$ cells upon Amiloride or Benzamil treatment (Figures S2M–S2O) or KD of αENaC (Figure S2P). Interestingly, αENaC also plays a role in differentiation as KD or blocking of ENaC significantly decreased the proportion of βIII-tubulin$^+$ neurons from primary cells (Figures 2L–2N and S2Q–S2S) or from neurospheres (Figures S3A–S3F) and also after shorter (6 hr) incubation in the ENaC blockers (Figures S3G–S3I). Noteworthy, pharmacological block by Benzamil showed effects additive to αENaC KD (Figures S2T–S2X), suggesting either non-specific pharmacological effects or incomplete genetic removal of ENaC. Taken together, limiting ENaC function or protein *in vitro* impairs survival, proliferation, and neurogenesis.

Conditional Deletion of αENaC In NSCs *In Vivo* Reduces SEZ Cell Number and Proliferation

Next, we examined the role of αENaC *in vivo* by deleting αENaC selectively in NSCs and their progeny using GLAST^{CreERT2}/CAG-GFP mice (Mori et al., 2006; Nakamura et al., 2006) crossed with Scnn1a$^{flox/flox}$ mice (as gene Scnn1a encodes αENaC; (Hummler et al., 2002) to obtain GLAST^{CreERT2}/CAG-GFP/Scnn1a$^{wt/wt}$ (control) and GLAST^{CreERT2}/CAG-GFP/Scnn1a$^{flox/flox}$ (iENaC) knockout (KO) mice. Injections of tamoxifen, Tam (Petrik et al., 2012) lead to deletion of Scnn1a and GFP expression in GLAST-expressing cells and their progeny. First, we examined at what time point ENaC protein is lost in the recombined SEZ cells at different times after induction. At 5 days post Tam (DPT), the proportion of αENaC$^+$ cells among recombined GFP$^+$ cells was already reduced in iENaC KO but reached even lower levels by 10 DPT with only about 5% of GFP$^+$ ENaC$^+$ cells left (Figures S4A–S4C). Therefore, we chose to examine this time point for a phenotype.

We performed stereological and proportional analyses of GFP$^+$ cells double stained for Ki67 and DCX at 10 DPT (Figures 3A and 3B). Consistent with the *in vitro* results, the absolute number of GFP$^+$ cells was reduced in the iENaC KO SEZ versus control (Figure 3C). As the reduction in GFP$^+$ cells may be due to a lower recombination rate, we determined the recombination efficiency by assessing the number of recombined GFP$^+$ astrocytes in the cerebral cortex gray matter (that are ENaC-negative and hence should not be affected, see Figure S1H). The recombined cell numbers at 10 DPT were well comparable in control and iENaC KO cerebral cortex (Figures S4D–S4F), suggesting a similar level of recombination efficiency between genotypes. Indeed, the decrease in recombined cells resulted in reduced SEZ thickness (measured as the dense band of DAPI$^+$ cells directly adjacent to the lateral ventricle) in iENaC KO compared to controls (Figure 3E). Importantly, these results also indicate that the phenotype in the recombined cells is not compensated by surrounding non-targeted cells.

Next, we examined whether GFP$^+$ cells in iENaC KO were reduced by defects in proliferation, survival, or fate change. We found fewer proliferating cells (Ki67$^+$GFP$^+$), both progenitors (Ki67$^+$DCX-GFP$^+$) and proliferating neuroblasts (Ki67$^+$DCX$^+$ GFP$^+$) in the SEZ of iENaC KO compared to control (Figure 3C), while non-proliferating (Ki67$^-$) neuroblasts were not significantly affected in their number. Likewise, the proportion of progenitors and proliferating and non-proliferating neuroblasts among GFP$^+$ cells showed a significant reduction of all proliferating cells (progenitors and proliferating neuroblasts), while the other populations were relatively less affected in iENaC KO versus control (Figure 3D), emphasizing the effect of ENaC deletion on proliferation.

To determine whether NSC numbers are reduced, we discriminated Sox2$^+$ GFAP$^-$ progenitors and Sox2$^+$GFAP$^+$ NSCs (Figure 3F). Indeed, the NSC number was significantly reduced in the iENaC KO SEZ (Figure 3G), suggesting that both NSCs and their proliferating progeny are affected by αENaC ablation.

To address whether the reduction in NSCs may be due to an altered fate, we quantified ependymal cells by S100β staining and their position lining the ventricle (Figure 3H). However, their proportion was similar between control and iENaC KO (Figure 3I), suggesting that the reduction in NSCs is not due to conversion into ependyma (Conover et al., 2000); for label-retaining cell measurements, see below. As staining for activated caspase 3 (Figures S4G and 3J), detecting cells in apoptosis, and for TUNEL (Figures S4H and S4I), detecting also cells dying by necroptosis and ferroptosis, showed no significant increase in cell death in iENaC KO at both 5 and 10 DPT, the *in vivo* phenotype seems mostly to result from reduced proliferation. Importantly, ENaC deletion also reduced the number of GFP$^+$ neurons in the iENaC KO compared to control OB (Figures 3K–3M), highlighting its key role in regulating adult neurogenesis.

ENaC Deletion *In Vivo* Affects NSC Activation and Cannot Be Compensated at Later Stages

Next, we examined the SEZ at 30 DPT (Figure 4). As expected, we found a larger number of GFP$^+$ cells in the control SEZ compared to 10 DPT as further progeny has been generated from NSCs (Figures 4A and 4B). Conversely, in the iENaC KO SEZ there was virtually no increase in GFP$^+$ cell number during these additional 20 days (compare Figures 3C and 4C). Indeed, proliferation was drastically reduced at 30 DPT (Figures 4A–4D). To determine whether this is due to a depletion of NSCs by cell death and/or proliferation, we provided bromodeoxyuridine (BrdU), a thymidine analog, in drinking water for 2 weeks followed by a week of BrdU-free water. Then, Tam was administered and followed by another thymidine analog, EdU, in drinking water for a week. The analysis of GFP$^+$GFAP$^+$ and BrdU$^+$ or EdU$^+$ NSCs was performed at 7 DPT (19 days after BrdU, Figures 4E and 4F). The proportion of NSCs proliferating after ENaC deletion (EdU$^+$GFAP$^+$GFP$^+$) was significantly reduced in iENaC KO compared to control, whereas the proportion of NSCs proliferating before (BrdU$^+$GFAP$^+$GFP$^+$) was not (Figure 4G). This suggests that ENaC loss leads to reduced proliferation of NSCs, while NSCs that were dividing (and incorporating BrdU) before ENaC loss were not affected. Also, we observed a reduction in proportion of BrdU$^+$GFAP$^+$GFP$^+$ cells in iENaC KO when animals were given BrdU for 2 weeks after Tam and killed 1 week post BrdU (data not shown), supporting the notion that mostly NSC proliferation is affected by ENaC KO, even though we cannot fully rule out cell death or migration out of the niche as contributing to the severe depletion of NSCs. As a consequence of this depletion, the number of newly generated neurons also remains significantly reduced in the OB of iENaC KO compared to control (Figures 4H–4J), demonstrating the long-term severe effects of ENaC deletion on adult neurogenesis.

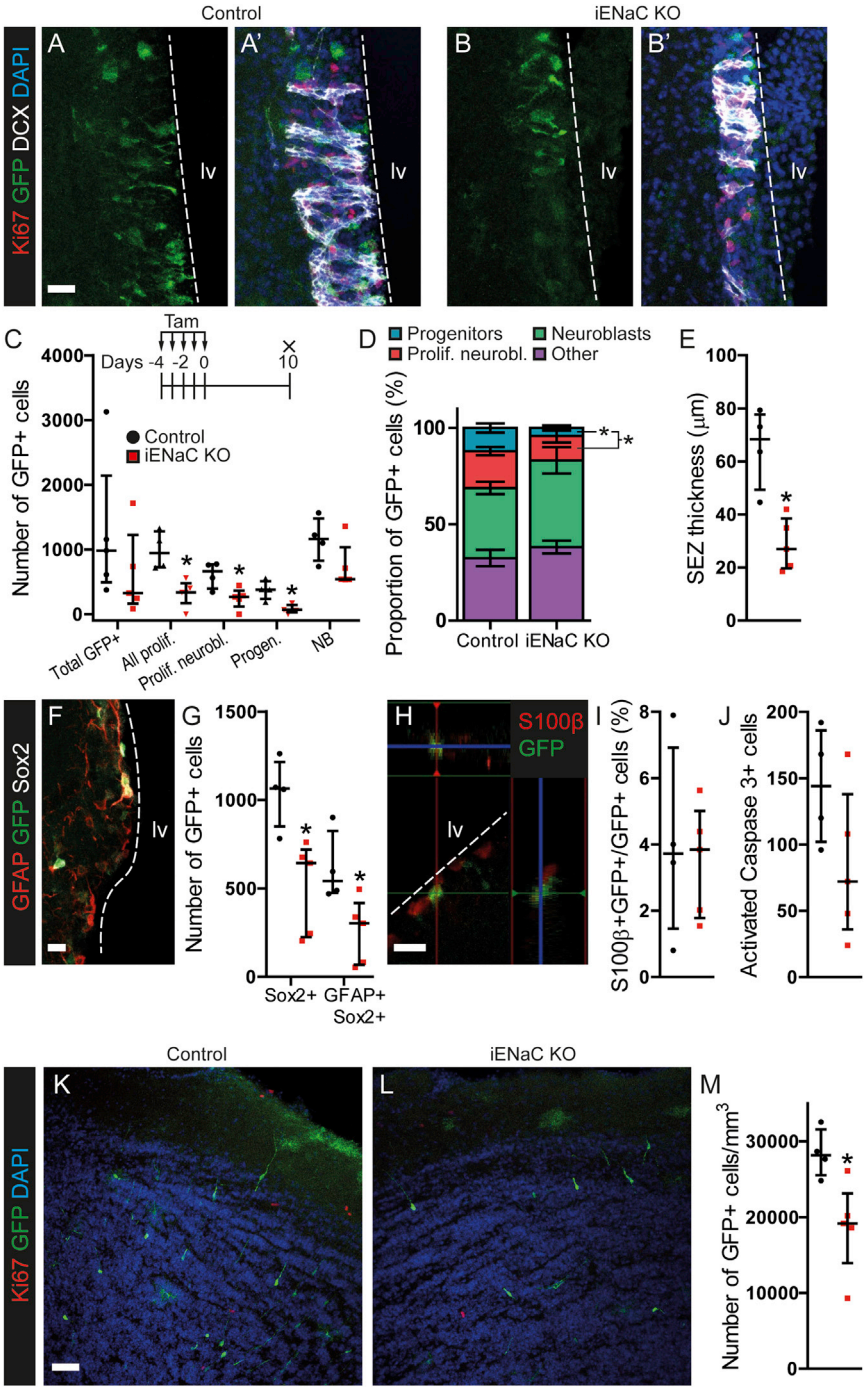

Figure 3. Phenotype of iENaC KO in GLAST-Expressing NSCs and Their Progeny in SEZ at 10 Days after Tamoxifen

(A and B) Representative images of SEZ from control (A) or iENaC KO (B) brains immunostained as indicated.

(C) Stereological analysis of absolute number of GFP$^+$ cell subpopulations in SEZ: all proliferating cells (Ki67$^+$), proliferating neuroblasts (Ki67$^+$ DCX$^+$), progenitors (Ki67$^+$DCX$^-$), and postmitotic neuroblasts (Ki67-DCX$^+$).

(D) Proportional analysis of Ki67$^+$ and/or DCX$^+$ cells in the GFP$^+$ cell population in control or iENaC KO.

(E) Measurements of average SEZ thickness in micrometers.

(F) Representative image of SEZ stained for GFAP, GFP, and Sox2.

(G) Quantification of number of Sox2$^+$GFP$^+$ progenitors and Sox2$^+$GFAP$^+$GFP$^+$ NSCs.

(H) Representative image of staining for S100β$^+$ and GFP$^+$ ependymal cells in SEZ.

(I) Proportion of S100β$^+$GFP$^+$ cells among GFP$^+$ cells in control and iENaC KO mice.

(J) Number of activated caspase 3 (AC3)-positive cells in both genotypes.

(K and L) Representative images of the OB stained as indicated in control (K) or iENaC KO (L).

(M) Quantification of number of GFP$^+$ cells per cubic millimeter of OB tissue.

lv, lateral ventricle. Scale bars, 50 μm in (A), (B), (K), and (L) and 20 μm in (F) and (H). Animals were tested at 9–10 weeks of age, n = 4–5. *p < 0.05; **p < 0.01. Data are presented as median ±IQR.

compared to WT mice (Figures S5A–S5C), demonstrating a very fast effect of αENaC loss on progenitor proliferation without affecting the proportion of apoptotic cells (Figures S5D and S5E). Thus, the iENaC KO phenotype is not exclusively due to the reduction in aNSC numbers but involves direct effects on proliferation of fast progenitors and neuroblasts.

αENaC Is Required in Fast Proliferating SEZ Progenitors *In Vivo* as Revealed by Their Selective Targeting

To discriminate between the effects of ENaC deletion in NSCs and their progeny, we selectively targeted the rapidly proliferating progenitor cells by murine leukemia virus (MLV)-based retroviral delivery of nuclear localization signal (NLS)-Cre recombinase (Colak et al., 2008) injected into the SEZ of ENaC$^{wt/wt}$/CAG-GFP (wild-type [WT]) and ENaC$^{flox/flox}$/CAG-GFP mice. Already 3 days post injection (dpi) Ki67$^+$ cells were reduced to almost half among all GFP$^+$ cells in the SEZ of ENaC$^{flox/flox}$, as

Fluid Flow Induces Proliferation in SEZ in an ENaC-Dependent Manner

ENaC channels are constitutively open, but their opening probability can be further increased by various mechanisms (Boscardin et al., 2016), including fluid flow (Fronius et al., 2010; Wang et al., 2009). To examine the effects of fluid flow, we used SEZ whole mounts and subjected them to control or elevated artificial cerebrospinal fluid (ACSF) flow (see STAR Methods and discussion for calculations of the shear stress being in the physiological range) for 4 hr (Figure 5A), after which the SEZ was stained and the number of Ki67$^+$ and DCX$^+$ cells was quantified (Figures 5B and 5C). Interestingly, the number of total Ki67$^+$ proliferating cells and proliferating neuroblasts was significantly increased in the SEZ whole mount exposed to elevated fluid flow

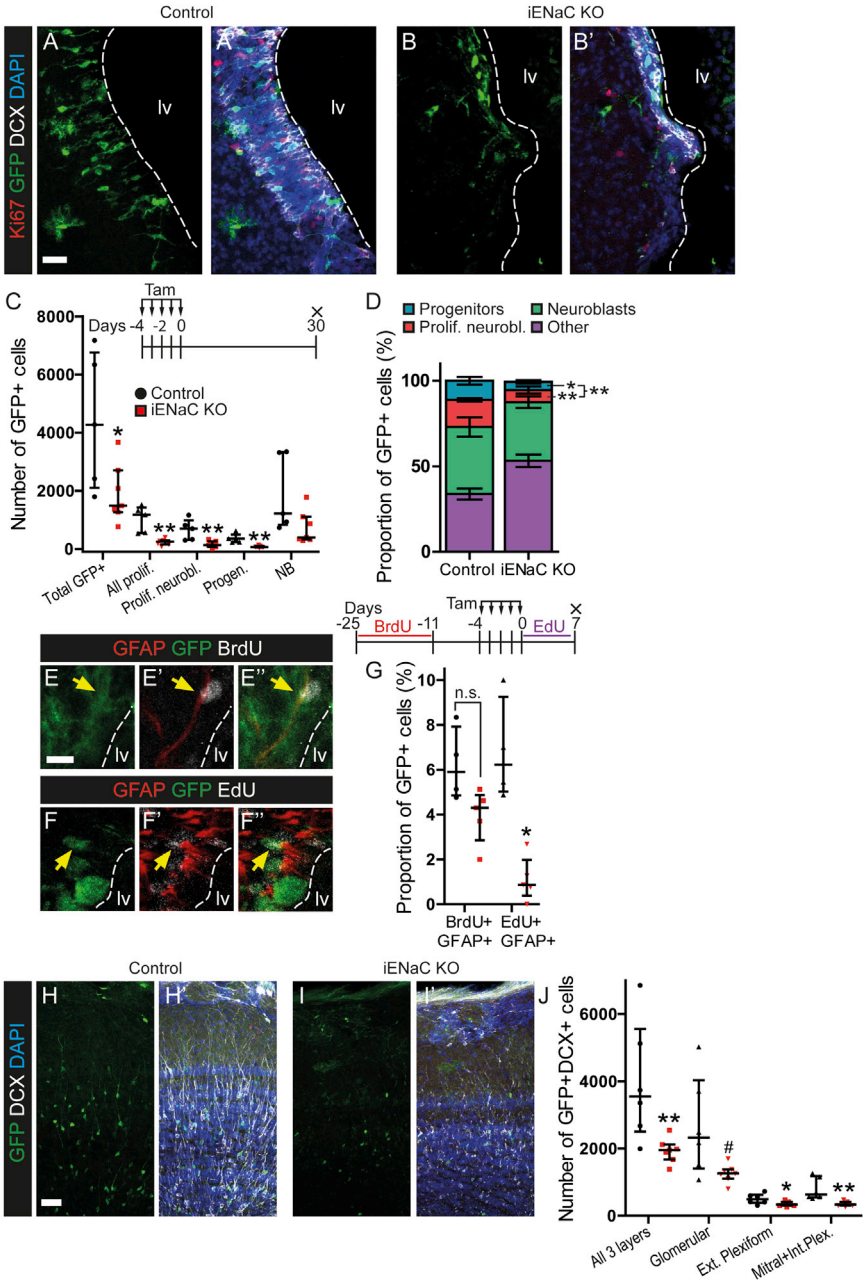

Figure 4. Phenotype of iENaC KO in SEZ at 30 Days after Tamoxifen

(A and B) Representative images of SEZ stained as indicated in control (A) and iENaC KO (B).

(C) Stereological quantification of GFP$^+$ cells labeled as in Figure 3C.

(D) Proportional analysis of Ki67$^+$ and/or DCX$^+$ GFP-expressing cells in SEZ of control or iENaC KO (D).

(E and F) SEZ stained for GFP, GFAP, and BrdU (E) or EdU (F); arrows point to triple-positive cells.

(G) Schematics of BrdU administration followed by BrdU chase, tamoxifen (Tam), EdU administration, and quantification of the proportion of GFP$^+$ GFAP$^+$ cells that had also incorporated BrdU or EdU.

(H and I) OB from Control (H) and iENaC KO (I) stained as indicated.

(J) Quantification of GFP$^+$ cells in different layers of OB cortex as indicated. Note that cell numbers were quantified by stereology, while in Figure 3M the cells were quantified in cubic millimeters of OB core tissue due to higher density of cells.

Scale bars, 50 μm in (A), (B), (H), and (I) and 10 μm in (E) and (G). Animals were tested at 11–13 weeks of age. n = 6–7 for Tam treated. n = 4–5 for BrdU treated. *p < 0.05; **p < 0.01. Data are presented as median ± IQR.

when compared to control (Figure 5D). Thus, increased flow induces a fast proliferation response.

To determine whether ENaC contributes to this response, we applied Benzamil that completely abrogated the flow-induced proliferation response (Figure 5D). Application of the high flow paradigm on the genetic mouse models showed an increase in proliferation only in GFP$^+$ cells in controls, but not in iENaC KO (Figures 5E–5G), clearly demonstrating that αENaC is required for this response.

To understand possible downstream signaling pathways mediating the proliferative response to the elevated fluid flow via ENaC, we considered the mitogen-activated protein kinases (Bodart, 2010) as prime candidates given their known involvement in SEZ stem cells activation (Ottone et al., 2014) and recent implication as mediators between mechanical stimuli and cell division (Gudipaty et al., 2017). SEZ whole mounts from WT mice were subjected to control or elevated ACSF flow as described above and stained for the activated (phosphorylated) form of Erk kinase (pErk; Figures 5H and 5I). High flow increased number of pErk$^+$ Ki67$^+$ and pErk$^+$ proliferating neuroblasts (Figure 5J). This increase was reversed in the presence of Benzamil suggesting that elevated fluid flow requires αENaC to activate Erk kinase. Furthermore, there was a smaller proportion and number of pErk$^+$GFP$^+$ cells in SEZ of iENaC KO compared to controls at 5 DPT (Figures S6F–S6H), underscoring the link between ENaC and downstream activation of the Erk kinase.

ENaC Loss Affects Flow-Induced Changes in Sodium and Calcium Dynamics in NSCs and Progenitors

To test whether high flow directly changes intracellular sodium via ENaC, we performed sodium imaging of the SEZ cells. Acute brain slices from control and iENaC KO mice at 21 DPT (Figures 6A and 6B) were bolus-loaded with sodium-binding benzofuran isophthalate-acetoxymethyl ester (SBFI-AM). SBFI-loaded cells were alternately excited at 340 and 380 nm, and changes in fluorescence emission were measured during baseline and high ACSF flow periods using ratiometric wide-field microscopy.

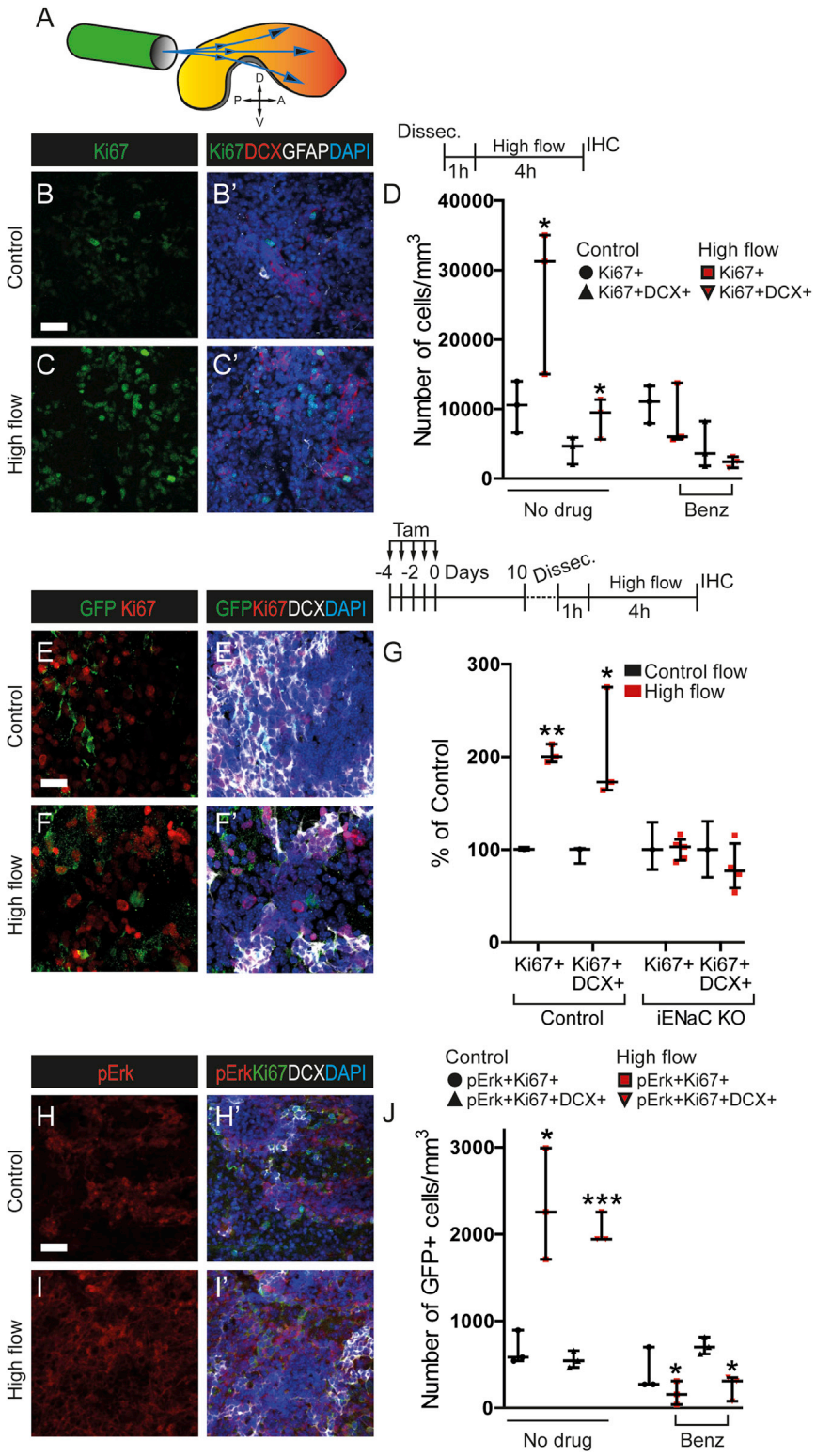

Figure 5. Effects of Fluid Flow on Cell Proliferation in SEZ

(A) Schematic depicting the experimental design for flow manipulation with SEZ whole mounts (anatomical directions: P, posterior; D, dorsal; A, anterior; V, ventral).

(B and C) Representative images of en-face SEZ stained as indicated after being subjected to control (B) or high (C) ACSF flow.

(D) Quantification of number of Ki67$^+$ and Ki67$^+$ DCX$^+$ (Proliferating Neuroblast) cells per cubic millimeter of SEZ tissue without or with Benzamil.

(E and F) Representative images of SEZ stained as indicated in iENaC KO mice at 10 DPT with control (E) and high fluid flow (F).

(G) Experimental design and cell quantification of proliferating cells and neuroblasts in control and iENaC KO mice under control and high flow.

(H and I) Representative images of SEZ stained as indicated with control (H) and high fluid flow (I).

(J) Quantification of pErk$^+$ cells per cubic millimeter of SEZ tissue without or with Benzamil.

Scale bars, 20 μm. Animals were tested at 7–10 weeks of age, n = 3–5. *p < 0.05; **p < 0.01. Data are presented as median ± IQR.

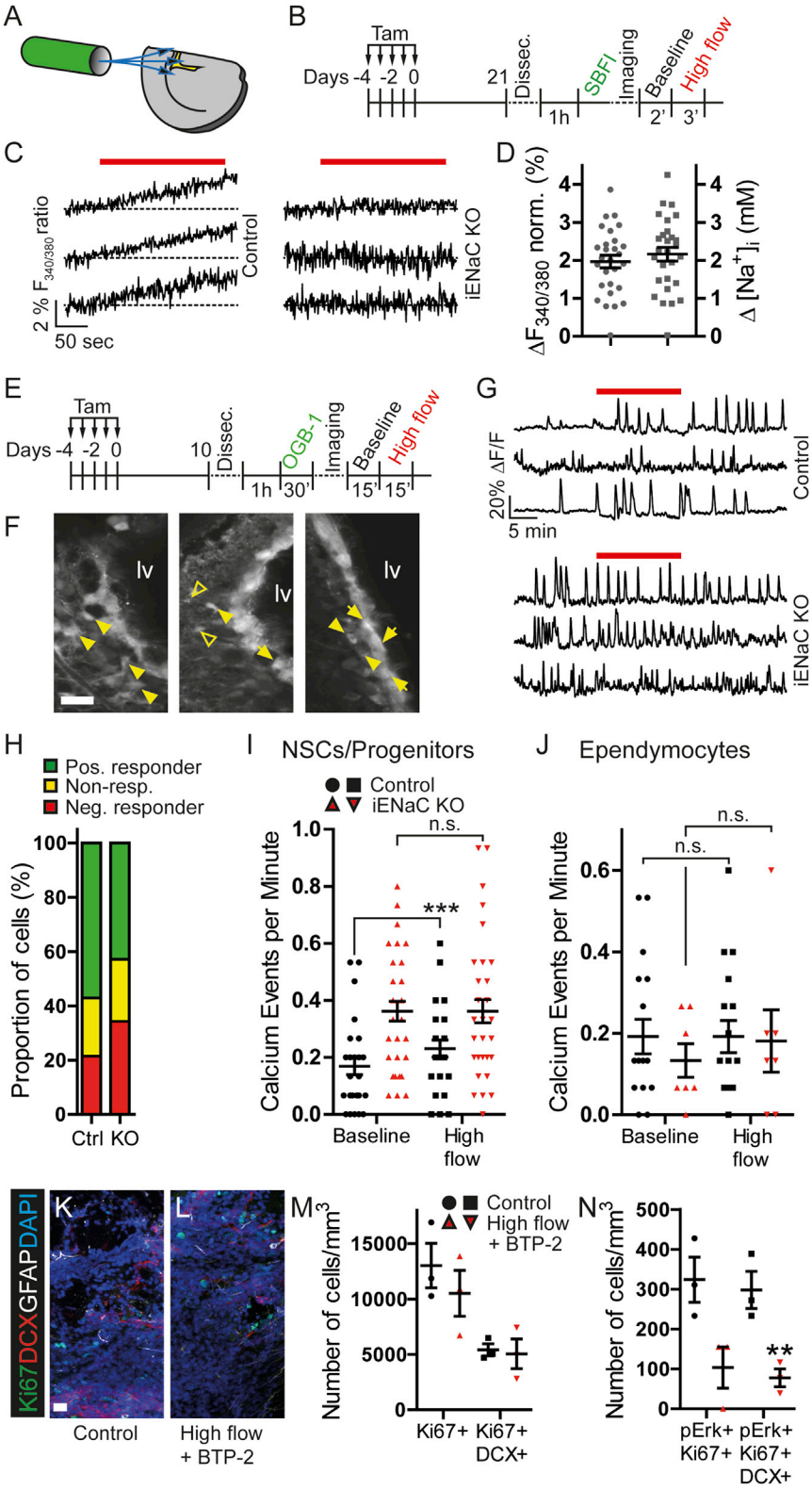

Figure 6. Sodium and Calcium Imaging in SEZ under Different Flow Conditions

(A) Schematic representation of an acute brain slice subjected to ACSF flow.

(B) The experimental design for sodium imaging.

(C) Representative traces of changes in SBFI fluorescence ratio as a function of time in SBFI-loaded SEZ cells. The red bar indicates exposure to high flow.

(D) The change in flow-induced SBFI fluorescence ratio and intracellular sodium concentration in control flow-responsive cells.

(E) The experimental design for calcium imaging.

(F) Representative still images of the OGB1-loaded cells in SEZ used for the calcium imaging.

(G) Stem/progenitor cells (full arrowhead), neuroblasts (empty arrowheads), ependymal cells (arrows). Representative traces of change in fluorescence (ΔF/F) as a function of time in OGB1-loaded SEZ cells from control and iENaC KO at 10 DPT. The red bar indicates exposure to high flow.

(H) Number of stem cells/progenitors sorted by their responsiveness to elevated fluid flow as indicated in the legend in control and iENaC KO.

(I) Frequency of calcium events per minute in baseline or high flow in GFP^+ stem cells/progenitors of control and iENaC.

(J) Frequency of calcium events per minute in ependymocytes. Animals were tested at 9–10 weeks of age, n = 3–4.

(K and L) Representative images of en-face SEZ stained as indicated after being subjected to control (K) or high flow with BTP-2 (L).

(M) Quantification of number of $Ki67^+$ and $Ki67^+$ DCX^+ cells per cubic millimeter of SEZ tissue.

(N) Quantification of number of $pErk^+$ cells per cubic millimeter.

Scale bars, 20 μm. Animals were tested at 7–10 weeks of age, n = 3. *p < 0.05; **p < 0.01; ***p < 0.001. Data are presented as mean ± SEM (D, I, and J as they are normally distributed) or median ± IQR (M and N).

The ratio of the SBFI fluorescence (340/380 nm) was calculated and normalized to baseline (Figure 6C) as previously done for recordings in parenchymal astrocytes (Langer and Rose, 2009). In controls, 35% of cells (28 out of 80) showed increased fluorescence ratio with the increase in fluid flow, whereas this was not the case for any of the 51 cells imaged in iENaC KO. This difference in distribution of responsive cells is statistically significant ($p < 0.0001$, Fisher's exact test). In the control responsive cells, the fluorescence ratio increased by about 2% after the onset of the high flow (Figure 6D), which corresponds to an increase in the intracellular sodium concentration by about 2.2 mM (based on *in situ* calibrations as described earlier [Meier et al., 2006]). Taken together, these data show that fluid flow induces sodium influx in ENaC-dependent manner.

To further understand how ENaC may convey the information about the fluid flow to the cells, we conducted calcium imaging experiments. Acute brain slices were loaded with the calcium indicator Oregon Green Bapta 1 (OGB1) and calcium oscillations were monitored in baseline flow (Figure 6E) followed by elevated flow and the baseline recovery. In the post hoc analysis, we evaluated calcium events in GFP^+ cells that separated into cell classes by their morphology and anatomical location as NSCs/progenitors, neuroblasts, and ependymocytes (Figure 6F). When cells were classified into positive responders (showing higher frequency of calcium oscillations in elevated fluid flow), non-responders (no change in frequency), and negative responders (reduced frequency), we observed a trend toward more negative and non-responders in the GFP^+ NSCs/progenitors of iENaC KO compared to controls (Figures 6G and 6H). Importantly, the GFP^+ NSCs/progenitors from control mice displayed an increase in the frequency of calcium oscillation in response to elevated ACSF flow, a feature that was not observed iENaC KO (Figure 6I). Thus, our data show that cells lacking ENaC do not have the capacity to respond to increased flow by changing Ca signals.

Notably, however, cells from iENaC KO at 10 DPT showed higher frequency of Ca signals at baseline ACSF flow when compared with controls (Figures 6G and 6I). These results suggest that calcium signaling is dysregulated 10 days after loss of ENaC. While this increase in calcium signaling may be counter-intuitive because the absence of sodium inward conductance should promote hyperpolarization and thus attenuate calcium oscillations, the increase in frequency of Ca signals may well be due to secondary changes at 10 DPT. Importantly, αENaC involvement in calcium signals was specific to NSCs/progenitors because there was no difference in Ca signals between control and iENaC KO or between baseline and elevated flow in cells classified as ependymocytes (Figure 6J).

Next, we tested whether the shear stress specifically affects only cells facing the ventricle or its influence is projected also to cells located deeper in the niche. We loaded SEZ whole mounts from controls with OGB1 and recorded calcium events in the NSCs at the surface or deep in the tissue (Figures S6A–S6F). The pool of surface cells (33 total) contained statistically significantly more cells positively responding to high flow than the deeper cells (27 total, $p < 0.0001$, Fisher's exact test, Figure S6G). Indeed, high flow increased the frequency of calcium events only in the surface, but not the deep cells (Figure S6H), suggesting that contact with the ventricle is critical for cellular responsiveness to shear stress.

To identify the possible source of calcium, we exposed SEZ whole mounts to a specific blocker of the store-operated Ca-release-activated Ca (CRAC) channels, BTP-2 (YM-58483; [Parekh, 2010]), given the relatively slow nature of the flow-induced Ca signals. Similar to Benzamil (Figure 5D), BTP-2 also abrogated the flow-induced increase in proliferating cells or neuroblasts in SEZ (Figures 6K–6M), suggesting that CRAC channels are a likely source of calcium in this context. Finally, blocking of CRAC channels also abolished the flow-induced increase in the number of proliferating cells and proliferating neuroblasts positive for pErk (Figure 6N) suggesting that the activation of Erk kinase is downstream of CRAC (Chang et al., 2006).

DISCUSSION

αENaC Channel Activity Is a Key Regulator of the SEZ Neurogenic Activity

Here, we provide for the first time a role for a voltage- and ligand-independent ion channel in adult neurogenesis. Our results show that αENaC is expressed in NSCs and their progeny in the SEZ, where it is critical for their proliferation. In addition, we suggest that ENaC allows the NSCs to sense fluid flow as one mechanism regulating the neurogenic process.

While ENaC is an essential component of epithelial cells in the peripheral organs (Hanukoglu and Hanukoglu, 2016), this channel has hardly been studied in the brain, let alone in NSCs. Both qPCR and immunohistochemistry showed the predominant expression of the alpha subunit in both the SEZ tissue and in sorted NSCs and neuroblasts, which is the subunit essential for channel function. While ENaC channels have been suggested to exist in different stoichiometry *in vitro* (Anantharam and Palmer, 2007; Staruschenko et al., 2005), only channels containing αENaC, either alone or with other subunits can form functional channels (Canessa et al., 1993; McNicholas and Canessa, 1997). Indeed, ENaC subunits show different expression profiles in cell-dependent context. For example, colonic epithelia or Müller glia express α, but not β or γ ENaC subunits (Asher et al., 1996; Brockway et al., 2002) similar to our findings in NSCs. Thus, the lack of β or γ ENaC subunits does not preclude ENaC currents. Indeed, we recorded Benzamil-sensitive currents in Aldh1l1-GFP^+ cells with radial glia morphology suggesting functional ENaC currents in NSCs. Moreover, we show flow-induced Na signals only in the presence, but not absence of αENaC in SEZ cells. Our observation that ENaC blockers at high concentrations (Hirsh et al., 2004) were needed to induce proliferation deficits similar to αENaC KD *in vitro* is consistent with the native ENaC channels containing only α or β subunits being less sensitive to these blockers (McNicholas and Canessa, 1997). Importantly, however, αENaC is the subunit essential for channel function, which is why we targeted it for deletion here.

αENaC Regulates Proliferation of NSCs and Their Progeny

Our *in vitro* and *in vivo* results jointly point toward the conclusion that ENaC predominantly regulates cell proliferation in the SEZ. Blocking or knocking down ENaC in neurosphere-derived or primary SEZ cells decreases the proliferation as shown by live

imaging and immunostaining for Ki67$^+$. Similarly, knocking out αENaC in NSCs *in vivo* leads to fewer EdU$^+$ NSCs and their progeny in the SEZ. Furthermore, Cre delivered selectively to the rapidly proliferating cells by viral vectors (Colak et al., 2008) revealed that αENaC is also required for proliferation in progenitors and neuroblasts. Thus αENaC acts in a bimodal manner regulating proliferation of both actively dividing NSCs as well as their progeny. So far, only few reports link ENaC activity to cell-cycle progression. For example, blocking ENaC had anti-tumor effects (Matthews et al., 2011) and halted the cell cycle in G0/G1 phase (Rooj et al., 2012).

Notably, the effects of blocking or KD of ENaC *in vitro* included also cell death. However, we did not detect any statistically significant change in apoptotic cells at 5 or 10 DPT in iENaC KO and at 3 days post injection of retroviruses or any change in survival of quiescent NSCs labeled by BrdU prior to the ENaC deletion. The fact we did not observe increased cell death in the iENaC KO *in vivo* cannot rule out a possible contribution of cell death to the severe cellular depletion of the SEZ, but the fact that we could detect increased cell death upon ENaC deletion *in vitro*, but not *in vivo* suggests that some elements of the niche environment *in vivo* are helping to keep ENaC KO cells alive.

Fluid Flow Regulates Proliferation via ENaC in the Whole-Mount SEZ

Our findings that fluid flow stimulates cell proliferation in SEZ in an ENaC-dependent manner suggest that ENaC may serve as a sensor of environmental changes. Indeed, this sensory role for ENaC was previously suggested in taste, mechanosensing, or circumventricular organs of the brain (Chandrashekar et al., 2010; Miller and Loewy, 2013). The laminar shear stress elicited by fluid flow increases open probability and thus ENaC currents (Althaus et al., 2007; Karpushev et al., 2010), a phenomenon also observed in native tissues such as endothelial cells in blood vessels or tubules in kidney nephrons (Morimoto et al., 2006; Satlin et al., 2001; Wang et al., 2009).

But how does the shear stress applied here compare to the *in vivo* situation? To our knowledge, direct measurements of the shear stress forces in the lateral ventricle are not available, especially not in mice. In humans, various non-invasive clinical studies were conducted to estimate the CSF velocity (Cohen et al., 2009). Near the fluid-solid interface the velocity is estimated at 0.5–1 mm/s (Siyahhan et al., 2014; Yamada et al., 2013). However, the CSF velocities are much higher in the bulk fluid movement and can reach up to 5–8 cm/s under the influence of the cardiac and respiratory cycle phase (Battal et al., 2011; Öztürk et al., 2016). In our preparation, the ACSF velocity exiting the capillary is around 3 cm/s, which is within the velocity limits mentioned above. This flow velocity with forces previously shown to stimulate ENaC (Althaus et al., 2007) causes an increase in the intracellular sodium concentration in NSCs in control but not iENaC KO SEZ.

Moreover, the effects of increased fluid flow on proliferation are diminished by Benzamil in WT tissue or do not occur in GFP$^+$ cells lacking αENaC. Finally, the elevated fluid flow activates Erk kinase in ENaC-dependent fashion suggesting that it connects fluid flow with proliferation. Thus, our results not only imply for the very first time fluid flow and hence physical forces as a regulator of adult NSCs proliferation in the SEZ, but also identify the channel ENaC as the central mediator. This is important given the expression of various other mechanosensitive channels in NSCs, such as Piezo and TRP channels (Beckervordersandforth et al., 2010; Blumenthal et al., 2014; Codega et al., 2014), and the proposed role of mechanical forces in regulating *Drosophila* gut stem cells (He et al., 2018) or embryonic NSCs *in vitro* (Park et al., 2017).

Why would NSCs and progenitors need to sense fluid flow? One possibility is that sensing fluid flow may serve as an all-or-none mechanism to detect their presence at the surface of the ventricle. Indeed, our calcium imaging experiments from SEZ whole mounts support this idea as mostly cells at the surface of the ventricle exhibited increased frequency in Ca signals in response to changes in fluid flow, whereas deeper cells did not. We therefore suggest that SEZ cells utilize the constant fluid drag forces to sense their presence at the ventricle, rather than actually measuring fluid flow speed as do endothelial or kidney cells. Indeed, this is consistent with the concept that radial glial cells contacting the ventricle, but not those deeper in the SEZ, would act as NSCs (Lim and Alvarez-Buylla, 2016).

However, it is important to recognize that ENaC is also regulated by a wide variety of factors other than mechanical forces, such as extracellular proteases and ions or cytoplasmic kinases and links to the cytoskeleton (Boscardin et al., 2016), which may also be involved in its function in the SEZ. Indeed, reducing ENaC protein in conditions with negligible fluid flow, such as *in vitro* preparations, still affects proliferation and viability of NSCs and progenitor cells. We propose that the constitutively open ENaC channel contributes to the increase in membrane potential in proliferating cells (see, e.g., review by Swayne and Wicki-Stordeur, 2012). The NSCs have low resting membrane potential close to the potassium equilibrium potential of around −80 mV (Liu et al., 2006). However, prior to entering the cell cycle the membrane potential becomes more depolarized (Swayne and Wicki-Stordeur, 2012). Importantly, under normal electrochemical gradient for sodium as it is in NSCs, ENaC carries sodium influx into the cell with the capacity to depolarize the membrane (Bigiani and Cuoghi, 2007; Chifflet et al., 2005). Our data therefore suggest that the constant albeit small influx of sodium may contribute to the change in membrane potential required to initiate proliferation.

ENaC Function Bridges Fluid Flow and Calcium Signaling

Besides the upstream regulators of ENaC function, we also examined downstream effectors. We have found that ENaC deletion abrogates flow-dependent increase in intracellular sodium and changes calcium signaling in response to increased fluid flow. Likewise, blocking Orai/STIM CRAC channels abrogated the flow-induced increase in cell proliferation and reduced number of cells positive for phosphorylated Erk kinase. The calcium oscillations we recorded in the SEZ were relatively slow (lasting around ten seconds) consistent with time course of release from calcium sources (Toth et al., 2016) that were observed before in NSCs of the SEZ (Young et al., 2014).

These results propose the following effects downstream of ENaC. ENaC carries sodium influx into the cell, which depolarizes the membrane potential (Bigiani and Cuoghi, 2007; Chifflet et al., 2005) as discussed above. Increased ENaC activity, as

during the high flow conditions, thus proportionally increases sodium influx as shown by live imaging and hence leads to further membrane depolarization (Althaus et al., 2007; Wang et al., 2009). This stimulates calcium exchangers and channels that together with inositol tri-phosphate receptors increase the cytoplasmic calcium concentration (Concepcion and Feske, 2017; Justet et al., 2013). Indeed, it has been shown that sodium influx via ENaC can activate dendritic cells in a calcium-dependent manner (Barbaro et al., 2017). The changes in calcium signaling ultimately trigger repetitive emptying of intracellular calcium stores as well as activate CRAC channels (Parekh, 2010) that were found upstream of activation of Erk kinase to regulate cell proliferation (Chang et al., 2006, 2008). Specifically, changes in calcium signaling were able to influence stem cell activity (Deng et al., 2015) with CRAC channels regulating proliferation of neural progenitors from SEZ (Somasundaram et al., 2014). Furthermore, the calcium-dependent PKC-α can regulate Erk activity, which in turn regulates ENaC function (Eaton et al., 2014), providing another layer of complexity between the signaling factors. As pErk was found to both increase (Mustafa et al., 2008) and decrease ENaC function (Eaton et al., 2014), changes in Erk activation with the high flow or in iENaC KO may also be a part of feedback compensations.

ENaC exerts a powerful control on adult neurogenesis with severe reduction in NSC activation and TAP and neuroblast proliferation resulting in much reduced neuronal output in its absence. We therefore propose a key role of this channel in regulating adult SEZ neurogenesis. This could have medical repercussions since ENaC blockers are used as diuretics to treat certain types of hypertension, can cross the blood-brain or CSF barrier (Alvarez de la Rosa et al., 2013), and may hence have potent side effects on neurogenesis (Ernst et al., 2014). Our results emphasize how important it is to understand regulators of adult neurogenesis and highlight the importance of ion-mediated signaling for neural stem and progenitor behavior in the adult brain.

STAR★METHODS

Detailed methods are provided in the online version of this paper and include the following:

- KEY RESOURCES TABLE
- CONTACT FOR REAGENT AND RESOURCE SHARING
- EXPERIMENTAL MODEL AND SUBJECT DETAILS
  - Mice
  - Cell Cultures
- METHOD DETAILS
  - Cell Cultures *In Vitro*
  - RT-qPCR
  - BrdU and EdU Experiments
  - Immunohistochemistry
  - Retroviral Cre delivery for Knock-out of ENaC in Fast Proliferating SEZ Cells *In Vivo*
  - Stereologic and Proportional Analyses
  - Electrophysiology
  - Shear Stress Experiments
  - Sodium Imaging
  - Calcium Imaging
- STATISTICAL ANALYSIS
- DATA AND SOFTWARE AVAILABILITY

SUPPLEMENTAL INFORMATION

Supplemental Information includes six figures and one table and can be found with this article online at https://doi.org/10.1016/j.stem.2018.04.016.

ACKNOWLEDGMENTS

We are particularly thankful to Edith Hummler for allowing the use of the floxed alpha ENaC mice (Scnn1a/Tm1.1) and to James D. Stockand for providing expression vectors containing cDNA of mouse ENaC subunits. We are also very grateful to Gabriela Jäger, Tatiana Simon-Ebert, Manja Thorwirth, and Detlef Franzen for their excellent technical help and to the viral vector facility of the SFB 870 (TPZ04 funded by DFG). This project was funded in part by the Marie Curie Fellowship (PIIF-GA-2013-628603) to D.P., DFG collaborative research center "SFB 870: Assembly and Function of Neuronal Circuits" to M.G. (CRC870/TP-A06) and B.G. (CRC870/TPB06), the German Excellence Initiative (Graduate School of Systemic Neurosciences, LMU, GSN 82, and EXC1010 Synergy), the priority program 1757 (Go13/1-2) to M.G. and C.R.R. (Ro2327/8-2), and the priority program 1738 and the advanced ERC grant "ChroNeuroRepair" (340793) to M.G.

AUTHOR CONTRIBUTIONS

M.G. conceived the project. D.P. and M.G. conceptualized the project. D.P., S.G., M.H.M., B.G., and M.G. designed experiments. D.P. performed all experiments and analyzed all results other than the following: S.G. performed stereotaxic surgeries; M.P. performed FACS sorting; D.P. and M.H.M. performed experiments and analyzed results for calcium imaging; and N.J.G. and C.R.R. performed experiments and analyzed results for sodium imaging. D.P. and M.G. wrote the paper with feedback from the co-authors.

DECLARATION OF INTERESTS

The authors declare no competing interests.

Received: May 15, 2017
Revised: February 16, 2018
Accepted: April 17, 2018
Published: May 17, 2018

REFERENCES

Althaus, M., Bogdan, R., Clauss, W.G., and Fronius, M. (2007). Mechanosensitivity of epithelial sodium channels (ENaCs): Laminar shear stress increases ion channel open probability. FASEB J. *21*, 2389–2399.

Alvarez de la Rosa, D., Navarro-González, J.F., and Giraldez, T. (2013). ENaC modulators and renal disease. Curr. Mol. Pharmacol. *6*, 35–43.

Amin, M.S., Wang, H.W., Reza, E., Whitman, S.C., Tuana, B.S., and Leenen, F.H. (2005). Distribution of epithelial sodium channels and mineralocorticoid receptors in cardiovascular regulatory centers in rat brain. Am. J. Physiol. Regul. Integr. Comp. Physiol. *289*, R1787–R1797.

Anantharam, A., and Palmer, L.G. (2007). Determination of epithelial Na+ channel subunit stoichiometry from single-channel conductances. J. Gen. Physiol. *130*, 55–70.

Asher, C., Wald, H., Rossier, B.C., and Garty, H. (1996). Aldosterone-induced increase in the abundance of Na+ channel subunits. Am. J. Physiol. *271*, C605–C611.

Barbaro, N.R., Foss, J.D., Kryshtal, D.O., Tsyba, N., Kumaresan, S., Xiao, L., Mernaugh, R.L., Itani, H.A., Loperena, R., Chen, W., et al. (2017). Dendritic cell amiloride-sensitive channels mediate sodium-induced inflammation and hypertension. Cell Rep. *21*, 1009–1020.

Battal, B., Kocaoglu, M., Bulakbasi, N., Husmen, G., Tuba Sanal, H., and Tayfun, C. (2011). Cerebrospinal fluid flow imaging by using phase-contrast MR technique. Br. J. Radiol. *84*, 758–765.

Beckervordersandforth, R., Tripathi, P., Ninkovic, J., Bayam, E., Lepier, A., Stempfhuber, B., Kirchhoff, F., Hirrlinger, J., Haslinger, A., Lie, D.C., et al. (2010). In vivo fate mapping and expression analysis reveals molecular hallmarks of prospectively isolated adult neural stem cells. Cell Stem Cell *7*, 744–758.

Bigiani, A., and Cuoghi, V. (2007). Localization of amiloride-sensitive sodium current and voltage-gated calcium currents in rat fungiform taste cells. J. Neurophysiol. *98*, 2483–2487.

Blumenthal, N.R., Hermanson, O., Heimrich, B., and Shastri, V.P. (2014). Stochastic nanoroughness modulates neuron-astrocyte interactions and function via mechanosensing cation channels. Proc. Natl. Acad. Sci. USA *111*, 16124–16129.

Bodart, J.F. (2010). Extracellular-regulated kinase-mitogen-activated protein kinase cascade: Unsolved issues. J. Cell. Biochem. *109*, 850–857.

Boscardin, E., Alijevic, O., Hummler, E., Frateschi, S., and Kellenberger, S. (2016). The function and regulation of acid-sensing ion channels (ASICs) and the epithelial Na(+) channel (ENaC): IUPHAR Review 19. Br. J. Pharmacol. *173*, 2671–2701.

Brockway, L.M., Zhou, Z.H., Bubien, J.K., Jovov, B., Benos, D.J., and Keyser, K.T. (2002). Rabbit retinal neurons and glia express a variety of ENaC/DEG subunits. Am. J. Physiol. Cell Physiol. *283*, C126–C134.

Butt, A.M., and Kalsi, A. (2006). Inwardly rectifying potassium channels (Kir) in central nervous system glia: A special role for Kir4.1 in glial functions. J. Cell. Mol. Med. *10*, 33–44.

Canessa, C.M., Horisberger, J.D., and Rossier, B.C. (1993). Epithelial sodium channel related to proteins involved in neurodegeneration. Nature *361*, 467–470.

Chandrashekar, J., Kuhn, C., Oka, Y., Yarmolinsky, D.A., Hummler, E., Ryba, N.J., and Zuker, C.S. (2010). The cells and peripheral representation of sodium taste in mice. Nature *464*, 297–301.

Chang, W.C., Nelson, C., and Parekh, A.B. (2006). Ca2+ influx through CRAC channels activates cytosolic phospholipase A2, leukotriene C4 secretion, and expression of c-fos through ERK-dependent and -independent pathways in mast cells. FASEB J. *20*, 2381–2383.

Chang, W.C., Di Capite, J., Singaravelu, K., Nelson, C., Halse, V., and Parekh, A.B. (2008). Local Ca2+ influx through Ca2+ release-activated Ca2+ (CRAC) channels stimulates production of an intracellular messenger and an intercellular pro-inflammatory signal. J. Biol. Chem. *283*, 4622–4631.

Chifflet, S., Hernández, J.A., and Grasso, S. (2005). A possible role for membrane depolarization in epithelial wound healing. Am. J. Physiol. Cell Physiol. *288*, C1420–C1430.

Codega, P., Silva-Vargas, V., Paul, A., Maldonado-Soto, A.R., Deleo, A.M., Pastrana, E., and Doetsch, F. (2014). Prospective identification and purification of quiescent adult neural stem cells from their in vivo niche. Neuron *82*, 545–559.

Cohen, B., Voorhees, A., Vedel, S., and Wei, T. (2009). Development of a theoretical framework for analyzing cerebrospinal fluid dynamics. Cerebrospinal Fluid Res. *6*, 12.

Colak, D., Mori, T., Brill, M.S., Pfeifer, A., Falk, S., Deng, C., Monteiro, R., Mummery, C., Sommer, L., and Götz, M. (2008). Adult neurogenesis requires Smad4-mediated bone morphogenic protein signaling in stem cells. J. Neurosci. *28*, 434–446.

Concepcion, A.R., and Feske, S. (2017). Regulation of epithelial ion transport in exocrine glands by store-operated Ca^{2+} entry. Cell Calcium *63*, 53–59.

Conover, J.C., Doetsch, F., Garcia-Verdugo, J.M., Gale, N.W., Yancopoulos, G.D., and Alvarez-Buylla, A. (2000). Disruption of Eph/ephrin signaling affects migration and proliferation in the adult subventricular zone. Nat. Neurosci. *3*, 1091–1097.

Deng, H., Gerencser, A.A., and Jasper, H. (2015). Signal integration by Ca(2+) regulates intestinal stem-cell activity. Nature *528*, 212–217.

Doetsch, F., García-Verdugo, J.M., and Alvarez-Buylla, A. (1997). Cellular composition and three-dimensional organization of the subventricular germinal zone in the adult mammalian brain. J. Neurosci. *17*, 5046–5061.

Dyka, F.M., May, C.A., and Enz, R. (2005). Subunits of the epithelial sodium channel family are differentially expressed in the retina of mice with ocular hypertension. J. Neurochem. *94*, 120–128.

Eaton, A.F., Yue, Q., Eaton, D.C., and Bao, H.F. (2014). ENaC activity and expression is decreased in the lungs of protein kinase C-α knockout mice. Am. J. Physiol. Lung Cell. Mol. Physiol. *307*, L374–L385.

Enuka, Y., Hanukoglu, I., Edelheit, O., Vaknine, H., and Hanukoglu, A. (2012). Epithelial sodium channels (ENaC) are uniformly distributed on motile cilia in the oviduct and the respiratory airways. Histochem. Cell Biol. *137*, 339–353.

Ernst, A., Alkass, K., Bernard, S., Salehpour, M., Perl, S., Tisdale, J., Possnert, G., Druid, H., and Frisén, J. (2014). Neurogenesis in the striatum of the adult human brain. Cell *156*, 1072–1083.

Fischer, J., Beckervordersandforth, R., Tripathi, P., Steiner-Mezzadri, A., Ninkovic, J., and Götz, M. (2011). Prospective isolation of adult neural stem cells from the mouse subependymal zone. Nat. Protoc. *6*, 1981–1989.

Fricke, B., Lints, R., Stewart, G., Drummond, H., Dodt, G., Driscoll, M., and von Düring, M. (2000). Epithelial Na+ channels and stomatin are expressed in rat trigeminal mechanosensory neurons. Cell Tissue Res. *299*, 327–334.

Fronius, M., Bogdan, R., Althaus, M., Morty, R.E., and Clauss, W.G. (2010). Epithelial Na+ channels derived from human lung are activated by shear force. Respir. Physiol. Neurobiol. *170*, 113–119.

Fukuda, S., Kato, F., Tozuka, Y., Yamaguchi, M., Miyamoto, Y., and Hisatsune, T. (2003). Two distinct subpopulations of nestin-positive cells in adult mouse dentate gyrus. J. Neurosci. *23*, 9357–9366.

Giraldez, T., Afonso-Oramas, D., Cruz-Muros, I., Garcia-Marin, V., Pagel, P., González-Hernández, T., and Alvarez de la Rosa, D. (2007). Cloning and functional expression of a new epithelial sodium channel delta subunit isoform differentially expressed in neurons of the human and monkey telencephalon. J. Neurochem. *102*, 1304–1315.

Gleeson, J.G., Lin, P.T., Flanagan, L.A., and Walsh, C.A. (1999). Doublecortin is a microtubule-associated protein and is expressed widely by migrating neurons. Neuron *23*, 257–271.

Gudipaty, S.A., Lindblom, J., Loftus, P.D., Redd, M.J., Edes, K., Davey, C.F., Krishnegowda, V., and Rosenblatt, J. (2017). Mechanical stretch triggers rapid epithelial cell division through Piezo1. Nature *543*, 118–121.

Hanukoglu, I., and Hanukoglu, A. (2016). Epithelial sodium channel (ENaC) family: Phylogeny, structure-function, tissue distribution, and associated inherited diseases. Gene *579*, 95–132.

He, L., Si, G., Huang, J., Samuel, A.D.T., and Perrimon, N. (2018). Mechanical regulation of stem-cell differentiation by the stretch-activated Piezo channel. Nature *555*, 103–106.

Heintz, N. (2004). Gene expression nervous system atlas (GENSAT). Nat. Neurosci. *7*, 483.

Hirsh, A.J., Sabater, J.R., Zamurs, A., Smith, R.T., Paradiso, A.M., Hopkins, S., Abraham, W.M., and Boucher, R.C. (2004). Evaluation of second generation amiloride analogs as therapy for cystic fibrosis lung disease. J. Pharmacol. Exp. Ther. *311*, 929–938.

Hummler, E., Mérillat, A.M., Rubera, I., Rossier, B.C., and Beermann, F. (2002). Conditional gene targeting of the Scnn1a (alphaENaC) gene locus. Genesis *32*, 169–172.

Hyndman, R.J., and Fan, Y. (1996). Sample quantiles in statistical packages. Am. Stat. *50*, 361–365.

Justet, C., Evans, F., Vasilskis, E., Hernández, J.A., and Chifflet, S. (2013). ENaC contribution to epithelial wound healing is independent of the healing mode and of any increased expression in the channel. Cell Tissue Res. *353*, 53–64.

Karpushev, A.V., Ilatovskaya, D.V., and Staruschenko, A. (2010). The actin cytoskeleton and small G protein RhoA are not involved in flow-dependent activation of ENaC. BMC Res. Notes *3*, 210.

Lacar, B., Young, S.Z., Platel, J.C., and Bordey, A. (2010). Imaging and recording subventricular zone progenitor cells in live tissue of postnatal mice. Front. Neurosci. *4*. Published online July 19, 2010. https://doi.org/10.3389/fnins.2010.00043.

Langer, J., and Rose, C.R. (2009). Synaptically induced sodium signals in hippocampal astrocytes in situ. J. Physiol. *587*, 5859–5877.

Lehtinen, M.K., Zappaterra, M.W., Chen, X., Yang, Y.J., Hill, A.D., Lun, M., Maynard, T., Gonzalez, D., Kim, S., Ye, P., et al. (2011). The cerebrospinal fluid provides a proliferative niche for neural progenitor cells. Neuron *69*, 893–905.

Lim, D.A., and Alvarez-Buylla, A. (2016). The adult ventricular-subventricular zone (V-SVZ) and olfactory bulb (OB) neurogenesis. Cold Spring Harb. Perspect. Biol. Published online May 2, 2016. https://doi.org/10.1101/cshperspect.a018820.

Liu, X., Bolteus, A.J., Balkin, D.M., Henschel, O., and Bordey, A. (2006). GFAP-expressing cells in the postnatal subventricular zone display a unique glial phenotype intermediate between radial glia and astrocytes. Glia *54*, 394–410.

Liu, Y., Jiang, B.J., Zhao, R.Z., and Ji, H.L. (2016). Epithelial sodium channels in pulmonary epithelial progenitor and stem cells. Int. J. Biol. Sci. *12*, 1150–1154.

Livak, K.J., and Schmittgen, T.D. (2001). Analysis of relative gene expression data using real-time quantitative PCR and the 2(-Delta Delta C(T)) Method. Methods *25*, 402–408.

López-Juárez, A., Remaud, S., Hassani, Z., Jolivet, P., Pierre Simons, J., Sontag, T., Yoshikawa, K., Price, J., Morvan-Dubois, G., and Demeneix, B.A. (2012). Thyroid hormone signaling acts as a neurogenic switch by repressing Sox2 in the adult neural stem cell niche. Cell Stem Cell *10*, 531–543.

Matthews, H., Ranson, M., and Kelso, M.J. (2011). Anti-tumour/metastasis effects of the potassium-sparing diuretic amiloride: An orally active anti-cancer drug waiting for its call-of-duty? Int. J. Cancer *129*, 2051–2061.

McNicholas, C.M., and Canessa, C.M. (1997). Diversity of channels generated by different combinations of epithelial sodium channel subunits. J. Gen. Physiol. *109*, 681–692.

Meier, S.D., Kovalchuk, Y., and Rose, C.R. (2006). Properties of the new fluorescent Na+ indicator CoroNa Green: Comparison with SBFI and confocal Na+ imaging. J. Neurosci. Methods *155*, 251–259.

Miller, R.L., and Loewy, A.D. (2013). ENaC γ-expressing astrocytes in the circumventricular organs, white matter, and ventral medullary surface: Sites for Na+ regulation by glial cells. J. Chem. Neuroanat. *53*, 72–80.

Mirzadeh, Z., Merkle, F.T., Soriano-Navarro, M., Garcia-Verdugo, J.M., and Alvarez-Buylla, A. (2008). Neural stem cells confer unique pinwheel architecture to the ventricular surface in neurogenic regions of the adult brain. Cell Stem Cell *3*, 265–278.

Mirzadeh, Z., Doetsch, F., Sawamoto, K., Wichterle, H., and Alvarez-Buylla, A. (2010). The subventricular zone en-face: Wholemount staining and ependymal flow. J. Vis. Exp. Published online May 6, 2010. https://doi.org/10.3791/1938.

Mori, T., Tanaka, K., Buffo, A., Wurst, W., Kühn, R., and Götz, M. (2006). Inducible gene deletion in astroglia and radial glia–a valuable tool for functional and lineage analysis. Glia *54*, 21–34.

Morimoto, T., Liu, W., Woda, C., Carattino, M.D., Wei, Y., Hughey, R.P., Apodaca, G., Satlin, L.M., and Kleyman, T.R. (2006). Mechanism underlying flow stimulation of sodium absorption in the mammalian collecting duct. Am. J. Physiol. Renal Physiol. *291*, F663–F669.

Mustafa, S.B., Castro, R., Falck, A.J., Petershack, J.A., Henson, B.M., Mendoza, Y.M., Choudary, A., and Seidner, S.R. (2008). Protein kinase A and mitogen-activated protein kinase pathways mediate cAMP induction of alpha-epithelial Na+ channels (alpha-ENaC). J. Cell. Physiol. *215*, 101–110.

Nakamura, T., Colbert, M.C., and Robbins, J. (2006). Neural crest cells retain multipotential characteristics in the developing valves and label the cardiac conduction system. Circ. Res. *98*, 1547–1554.

Ninkovic, J., and Götz, M. (2015). How to make neurons—Thoughts on the molecular logic of neurogenesis in the central nervous system. Cell Tissue Res. *359*, 5–16.

Nolte, C., Matyash, M., Pivneva, T., Schipke, C.G., Ohlemeyer, C., Hanisch, U.K., Kirchhoff, F., and Kettenmann, H. (2001). GFAP promoter-controlled EGFP-expressing transgenic mice: A tool to visualize astrocytes and astrogliosis in living brain tissue. Glia *33*, 72–86.

Ortega, F., Costa, M.R., Simon-Ebert, T., Schroeder, T., Götz, M., and Berninger, B. (2011). Using an adherent cell culture of the mouse subependymal zone to study the behavior of adult neural stem cells on a single-cell level. Nat. Protoc. *6*, 1847–1859.

Ortega, F., Berninger, B., and Costa, M.R. (2013). Primary culture and live imaging of adult neural stem cells and their progeny. Methods Mol. Biol. *1052*, 1–11.

Ottone, C., Krusche, B., Whitby, A., Clements, M., Quadrato, G., Pitulescu, M.E., Adams, R.H., and Parrinello, S. (2014). Direct cell-cell contact with the vascular niche maintains quiescent neural stem cells. Nat. Cell Biol. *16*, 1045–1056.

Öztürk, M., Sığırcı, A., and Ünlü, S. (2016). Evaluation of aqueductal cerebrospinal fluid flow dynamics with phase-contrast cine magnetic resonance imaging in normal pediatric cases. Clin. Imaging *40*, 1286–1290.

Parekh, A.B. (2010). Store-operated CRAC channels: Function in health and disease. Nat. Rev. Drug Discov. *9*, 399–410.

Park, M.G., Jang, H., Lee, S.H., and Lee, C.J. (2017). Flow shear stress enhances the proliferative potential of cultured radial glial cells possibly via an activation of mechanosensitive calcium channel. Exp. Neurobiol. *26*, 71–81.

Petrik, D., Jiang, Y., Birnbaum, S.G., Powell, C.M., Kim, M.S., Hsieh, J., and Eisch, A.J. (2012). Functional and mechanistic exploration of an adult neurogenesis-promoting small molecule. FASEB J. *26*, 3148–3162.

Petrik, D., Yun, S., Latchney, S.E., Kamrudin, S., LeBlanc, J.A., Bibb, J.A., and Eisch, A.J. (2013). Early postnatal in vivo gliogenesis from nestin-lineage progenitors requires cdk5. PLoS ONE *8*, e72819.

Pologruto, T.A., Sabatini, B.L., and Svoboda, K. (2003). ScanImage: Flexible software for operating laser scanning microscopes. Biomed. Eng. Online *2*, 13.

Prüss, H., Dewes, M., Derst, C., Fernández-Klett, F., Veh, R.W., and Priller, J. (2011). Potassium channel expression in adult murine neural progenitor cells. Neuroscience *180*, 19–29.

Rooj, A.K., McNicholas, C.M., Bartoszewski, R., Bebok, Z., Benos, D.J., and Fuller, C.M. (2012). Glioma-specific cation conductance regulates migration and cell cycle progression. J. Biol. Chem. *287*, 4053–4065.

Satlin, L.M., Sheng, S., Woda, C.B., and Kleyman, T.R. (2001). Epithelial Na(+) channels are regulated by flow. Am. J. Physiol. Renal Physiol. *280*, F1010–F1018.

Sawamoto, K., Wichterle, H., Gonzalez-Perez, O., Cholfin, J.A., Yamada, M., Spassky, N., Murcia, N.S., Garcia-Verdugo, J.M., Marin, O., Rubenstein, J.L., et al. (2006). New neurons follow the flow of cerebrospinal fluid in the adult brain. Science *311*, 629–632.

Scholzen, T., and Gerdes, J. (2000). The Ki-67 protein: From the known and the unknown. J. Cell. Physiol. *182*, 311–322.

Silva-Vargas, V., Maldonado-Soto, A.R., Mizrak, D., Codega, P., and Doetsch, F. (2016). Age-dependent niche signals from the choroid plexus regulate adult neural stem cells. Cell Stem Cell *19*, 643–652.

Simon, C., Lickert, H., Götz, M., and Dimou, L. (2012). Sox10-iCreERT2: A mouse line to inducibly trace the neural crest and oligodendrocyte lineage. Genesis *50*, 506–515.

Sirko, S., Irmler, M., Gascón, S., Bek, S., Schneider, S., Dimou, L., Obermann, J., De Souza Paiva, D., Poirier, F., Beckers, J., et al. (2015). Astrocyte reactivity after brain injury: The role of galectins 1 and 3. Glia *63*, 2340–2361.

Siyahhan, B., Knobloch, V., de Zélicourt, D., Asgari, M., Schmid Daners, M., Poulikakos, D., and Kurtcuoglu, V. (2014). Flow induced by ependymal cilia dominates near-wall cerebrospinal fluid dynamics in the lateral ventricles. J. R. Soc. Interface *11*, 20131189.

Somasundaram, A., Shum, A.K., McBride, H.J., Kessler, J.A., Feske, S., Miller, R.J., and Prakriya, M. (2014). Store-operated CRAC channels regulate gene expression and proliferation in neural progenitor cells. J. Neurosci. *34*, 9107–9123.

Staruschenko, A., Adams, E., Booth, R.E., and Stockand, J.D. (2005). Epithelial Na+ channel subunit stoichiometry. Biophys. J. *88*, 3966–3975.

Swayne, L.A., and Wicki-Stordeur, L. (2012). Ion channels in postnatal neurogenesis: Potential targets for brain repair. Channels (Austin) *6*, 69–74.

Tashiro, A., Zhao, C., and Gage, F.H. (2006). Retrovirus-mediated single-cell gene knockout technique in adult newborn neurons in vivo. Nat. Protoc. *1*, 3049–3055.

Toth, A.B., Shum, A.K., and Prakriya, M. (2016). Regulation of neurogenesis by calcium signaling. Cell Calcium *59*, 124–134.

Van Huysse, J.W., Amin, M.S., Yang, B., and Leenen, F.H. (2012). Salt-induced hypertension in a mouse model of Liddle syndrome is mediated by epithelial sodium channels in the brain. Hypertension *60*, 691–696.

Wang, S., Meng, F., Mohan, S., Champaneri, B., and Gu, Y. (2009). Functional ENaC channels expressed in endothelial cells: A new candidate for mediating shear force. Microcirculation *16*, 276–287.

Yamada, S., Miyazaki, M., Yamashita, Y., Ouyang, C., Yui, M., Nakahashi, M., Shimizu, S., Aoki, I., Morohoshi, Y., and McComb, J.G. (2013). Influence of respiration on cerebrospinal fluid movement using magnetic resonance spin labeling. Fluids Barriers CNS *10*, 36.

Yamaguchi, M., Saito, H., Suzuki, M., and Mori, K. (2000). Visualization of neurogenesis in the central nervous system using nestin promoter-GFP transgenic mice. Neuroreport *11*, 1991–1996.

Young, S.Z., Lafourcade, C.A., Platel, J.C., Lin, T.V., and Bordey, A. (2014). GABAergic striatal neurons project dendrites and axons into the postnatal subventricular zone leading to calcium activity. Front. Cell. Neurosci. *8*, 10.

STAR★METHODS

KEY RESOURCES TABLE

REAGENT or RESOURCE	SOURCE	IDENTIFIER
Antibodies		
Anti-CD133-PE	eBioscience	Cat# 12-4301; RRID:AB_465849
Anti-O4-APC	Miltenyi Biotech	Cat# 130095891; RRID:AB_10828153
Anti-PSA-NCAM-PE	Miltenyi Biotech	Cat# 130093274; RRID:AB_1036069
Anti-Glial Fibrillary Acidic Protein	Dako	Cat# N1506; RRID:AB_10013482
Anti-Glial Fibrillary Acidic Protein	Sigma Aldrich	Cat# G3893; RRID:AB_477010
Anti-beta-III-Tubulin	Sigma Aldrich	Cat# T8660; RRID:AB_477590
Anti-Green Fluorescent Protein	Aves Labs	Cat# GFP-1020; RRID:AB_10000240
Anti-Doublecortin	Merck-Millipore	Cat# AB5910; RRID:AB_2230227
Anti-Ki67	Thermo Scientific	Cat# RM-9106-S0; RRID:AB_2341197
Anti-Ki67	eBioscience	Cat# 14-5698; RRID:AB_1085318
Anti-phospho-p44/42 MAPK (Erk1/2)	Cell Signaling	Cat# 4370; RRID:AB_2315112
Anti-Sox2	Santa Cruz Biotech	Cat# SC-17320; RRID:AB_2286684
Anti-S100β	Sigma Aldrich	Cat# S2532; RRID:AB_477499
Anti-Olig2	Merck-Millipore	Cat# AB9610; RRID:AB_570666
Anti-Activated Caspase 3	Merck-Millipore	Cat# AB3623; RRID:AB_91556
Anti-beta-Catenin	BD Biosciences	Cat# 310153; RRID:AB_397554
Anti-BrdU	AbCam	Cat# AB6326; RRID:AB_305426
Anti-alpha-ENaC	StressMarq	Cat# SPC-403D; RRID:AB_2570681
Chemicals, Peptides, and Recombinant Proteins		
EGF	GIBCO	Cat# PHG0311
bFGF	GIBCO	Cat# 13256029
Poly-D-Lysine	Sigma Aldrich	Cat# P0899
Poly-L-Ornitine	Sigma Aldrich	Cat# P4957
Laminin	Roche	Cat# 11243217001
Amiloride	Sigma Aldrich	Cat# A7410
Benzamil	Sigma Aldrich	Cat# B2417
BTP-2 (YM-58483)	Selleckchem	Cat# S8380
Tamoxifen	Sigma Aldrich	Cat# T5648
5-Bromo-2′-deoxyuridine	Sigma Aldrich	Cat# T5648
5-ethynyl-2′-deoxyuridine	Thermo Life Technologies	Cat# C10340
Oregon Green Bapta 1, AM	Thermo Life Technologies	Cat# O6807
Sulforhodamine 101	Sigma Aldrich	Cat# S7635
Alexa Fluor 594	Thermo Life Technologies	Cat #A20004
SBFI, AM	Thermo Life Technologies	Cat# S1263
EGF–Alexa Fluor 647	Life Technologies	Cat# E-35351
Critical Commercial Assays		
In Situ Cell Death Detection Kit	Roche	Cat# 12156792910
RNeasy Micro Kit	QIAGEN	Cat# 74004
SYBR Green Master Mix	Roche	Cat# 12602520
TSA Plus HPR Rhodamine System	Perkin Elmer	Cat# NEL747B001
Click-iT EdU Imaging Kit	Thermo Life Technologies	Cat# C10340

(*Continued on next page*)

Continued

REAGENT or RESOURCE	SOURCE	IDENTIFIER
Deposited Data		
Mendeley Data Set 1	This paper	https://doi.org/10.17632/kp7v8mkf3s.2
Mendeley Data Set 2	This paper	https://doi.org/10.17632/8brx3kx9ky.2
Experimental Models: Organisms/Strains		
C57BL/6	LMU animal facility	RRID:MGI:2386275
Nestin-GFP	(Yamaguchi et al., 2000)	RRID:IMSR_RBRC06355
hGFAP-GFP	(Nolte et al., 2001)	RRID:MGI:3581617
Aldh1l-GFP	(Heintz, 2004)	RRID:MMRRC_011015-UCD
GLAST^{CreERT2}	(Mori et al., 2006)	MGI:3830051
CAG-CAT-GFP	(Nakamura et al., 2006)	RRID:IMSR_JAX:024636
Scnn1a/tm1.1Hum	(Hummler et al., 2002)	RRID:MGI:2386275
Oligonucleotides		
See Table S1 for qPCR Primers and esiRNA	This paper	N/A
Recombinant DNA		
pCAG-Cre	(Tashiro et al., 2006)	N/A
Software and Algorithms		
ZEN	Zeiss	https://www.zeiss.com/microscopy
Timm's Tracking Tool	Schroder lab, ETH Zurich	https://www.bsse.ethz.ch/csd/software/ttt-and-qtfy.html
PatchMaster	HEKA Elektronik	http://www.heka.com/downloads/downloads_main.html
Igor Pro	WaveMetrics	https://www.wavemetrics.com/products/igorpro/igorpro.htm
OriginPro 8.5G Software	OriginLab Corporation	https://www.originlab.com/
ImageJ	National Institutes of Health	https://imagej.net/Downloads
Fiji	Lab. Optical & Comp. Instr.	https://fiji.sc/
MATLAB	MathWorks	https://www.mathworks.com/products/matlab.html
Prism	GraphPad Software	https://www.graphpad.com/scientific-software/prism/
Adobe Illustrator	Adobe	https://www.adobe.com/de/products/illustrator

CONTACT FOR REAGENT AND RESOURCE SHARING

As the Lead Contact, Magdalena Götz (Helmholtz Center Munich, Germany) is responsible for all reagent and resource requests. Please contact Magdalena Götz at magdalena.goetz@helmholtz-muenchen.de with requests and inquiries.

EXPERIMENTAL MODEL AND SUBJECT DETAILS

Mice

All experimental procedures in this study were performed in accordance with German and European Union guidelines and were approved by our institutional animal care committee and the government of upper Bavaria (Regierung von Oberbayern). Mice were housed in a 12:12 hour light-dark cycle. All mice were 6-15 weeks old. Surgeries were performed aseptically under anesthesia with a mixture of fentanyl (0.05 mg/kg, Janssen), midazolam (5 mg/kg, Roche) and medetomidine (0.5 mg/kg, Orion Pharma). After surgery, anesthesia was terminated with atipamezol (2.5 mg/kg, Orion Pharma), flumazenil (0.5 mg/kg, Hexal) and buprenorphin (0.01 mg/ml, RB Pharmaceuticals Limited). Carprofen (5 mg/kg, Pfizer) was administered as a postoperative analgesic. We generated transgenic mice that allow temporal and tissue-specific control of expression of alpha subunit for ENaC encoded by the Scnn1a gene. We crossed GLAST^{CreERT2} mice (Mori et al., 2006) with CAG-GFP reporter (Nakamura et al., 2006) and with alpha ENaC$^{flox/flox}$ mice (Scnn1a/Tm1.1 line generated by Edith Hummler, University of Lausanne, Switzerland; (Hummler et al., 2002) and rederived

from frozen embryos at the European Mouse Mutant Archive (TAAM-CRNS) in Orléans, France) to obtain GLAST$^{WT/CreERT2}$/CAG-GFP/ENaC$^{wt/wt}$ (control) and GLAST$^{WT/CreERT2}$/CAG-GFP/ENaC$^{flox/flox}$ (iENaC KO) mice. Mice were genotyped as described previously (Hummler et al., 2002) with αENaC forward primer = GTCACTGTGTGCACCCTTAA, αENaC reverse primer = GCACAAA GATCTTATCCACC. Administration of i.p. tamoxifen (Tam; Sigma, St. Louis, Missouri, USA) induces CreER^{T2} translocation to the nucleus, which excises exon 1 in Scnn1a gene and the stop signal in CAG-GFP cassette. The Tam administration leads to deletion of alpha subunit of ENaC gene and GFP expression in GLAST-expressing cells and their progeny. Adult mice (6-8 weeks old, n = 5 or more per each group) were given Tam (Sigma; in 10% ethanol and 90% corn oil; 150 mg/kg i.p. (Petrik et al., 2012) for 5 consecutive days and were killed 5, 10 or 30 days post Tam. Besides the inducible iENaC KO mice, also WT C57Bl6, nestin-GFP (Yamaguchi et al., 2000), hGFAP-GFP mice (Nolte et al., 2001), Sox10-CreERT2 mice (Simon et al., 2012), CAG-GFP mice (Nakamura et al., 2006) and Aldh1l1-GFP (Aldh1l1-GFP) mice (GENSAT Chori ID #BX1126; (Heintz, 2004)) were used for breeding, immunohistochemistry, electrophysiology or shear stress experiments as described below. All these animals were bred and kept in our animal facility.

Cell Cultures

Primary cell cultures were prepared from littermates of adult C57BL/6 mice (6-8 weeks old) as adherent primary cell cultures or as neurospheres. The subependymal zone (SEZ) was micro-dissected as previously described (Ortega et al., 2011).

SEZ from one animal per one cell line (N = 3 or more). The tissue was digested for 30 minutes in 37°C with trypsin (3.5 mg/5 ml; Sigma) and hyaluronidase (3.5 mg/ 5 ml, Sigma). After sucrose gradient centrifugation, the cells were resuspended in DMEM/F12 medium (GIBCO, Thermo Fisher Scientific, Waltham, MA, USA) supplemented with penicillin (100 units/ml), streptomycin (100 μg/ml, GIBCO), glutamate (2 mM, GIBCO), and B27 supplement (1:50, Thermo Fisher). For neurospheres or for cells dissociated from neurospheres, the medium was also supplemented with EGF and bFGF2 (both 10 ng/ml; GIBCO) every 3-4 days. The neurospheres were passaged with trypsin (0.05%) 2-3 times (once per week) and then single cells were plated onto poly-D-lysine(PDL)-coated (Sigma) coverslips at density of 50-70.000 per well in a 24-well plate. For differentiation, individual spheres were plated on poly-L-ornitine (Sigma) /laminin (Roche) - coated (PLO/LM) coverslips and primary SEZ cells were plated on PDL-coated coverslips. For neurospheres or primary SEZ cultures in differentiation conditions, no growth factors were added into the medium but 1% Fetal Bovine Serum (FBS). Cell identity was checked by immunocytochemistry (ICC) for proteins specific to different cell types as described in greater details in the following sections.

METHOD DETAILS

Cell Cultures *In Vitro*

Pharmacological Blocking or Knock-down of ENaC

After the cells or neurospheres attached to coverslips, they were exposed either to the ENaC blockers (Sigma) or transfected with esiRNA against transcripts from Scnn1a (Mission esiRNA, Sigma). The neurospheres were allowed to attach for 2-3 hours and the primary SVZ cells for 20 hours before the exposure. The cells were exposed to Amiloride in final concentration of 100, 200 or 500 μM (100 mM stock solution in water) or Benzamil in final concentration of 10, 50 or 100 μM (5 mM stock solution in water) for 24 hours in 37°C. After that, medium was replaced and cells kept for another 72 hours. In selected experiments, cells were exposed to the blockers for only 6 hours. After that, the cells were fixed with 4% PFA in PBS and stained. As a control, only the vehicle (water) was added to the wells. For transfection with esiRNA, a mixture of 0.3 μg of esiRNA against EGFP (as control) or against mouse Scnn1a transcripts (Sigma) and Lipofectamine 2000 (1:50, Life Technologies, Darmstadt, Germany) was prepared according to the manufacturer's instructions and cells were subjected to 16 μL of the mixture per 50 μL of OptiMEM medium (GIBCO) per well for 4 hours at 37°C. After the transfection, the medium was replaced by the proliferation or differentiation medium as described above. The cells were collected for immunocytochemisty (ICC) 72 hours later. As a transfection control, Lipofectamine alone or esiRNA against GFP was used.

Immunocytochemistry

Cells were stained in 1X PBS with 2% bovine serum albumin (BSA, Sigma) and 0.5% Triton-X overnight in 4°C using rabbit polyclonal anti-GFAP (1:1000, Dako, Hamburg, Germany) and mouse IgG2b anti-βIII-tubulin (1:500, Sigma) antibodies. After washout, the cells were stained with secondary antibodies (1:300) for 2 hours at room temperature and nuclei-stained with DAPI (1:1000, Roche, Munich, Germany). The cells were mounted using the Aqua-Poly/Mount reagent (Polysciences, Eppelheim, Germany). Systematic random visual fields of the stained cells were taken either on an epi-fluorescent or a confocal microscope (model LSM 710, Zeiss, Oberkochen, Germany) to quantify proportion of GFAP+DAPI+ and βIII-tubulin+DAPI+ cells over all DAPI+ cells. Also, cells were stained for terminal deoxynucleotidyl transferase dUTP nick end labeling (TUNEL) using a staining kit (Roche) to obtain proportion of apoptotic cells.

Time Lapse Imaging

Primary SEZ cells were plated on PDL-coated plastic wells and exposed to 50 μM Benzamil for 24 hours, or esiRNA (0.3 μg per well) for 4 hours as described above. After that, cells were continuously imaged as described previously (Ortega et al., 2013). Briefly, cells were kept in 37°C in 8% CO_2 and pictures were taken every 5 or 8 minutes for 85 hours or longer. In some experiments, primary cells were imaged for 25 hours before the imaging was briefly stopped and 50 μM Benzamil was added to the medium, after which the time-lapse imaging immediately resumed. After imaging, cells were stained for GFAP and βIII-tubulin and their immunocytochemical

phenotype was identified. In primary cells, clonal analysis of individual cells was performed by tracking derived progeny cells using the Timm's Tracking Tool software as described previously (Ortega et al., 2013).

RT-qPCR

Three WT adult mice were transcardially perfused with ice-cold PBS (about 20 ml) to remove blood from tissue. After that, tissue was microdissected from SEZ, olfactory bulbs (OB), sensory motor cortex, and cerebellum. Also, heart, kidney and liver were dissected. Tissue was flash frozen in liquid nitrogen and later homogenized by glass homogenizer (organs) or insulin-type syringe (brain tissue). Total RNA was isolated using the standard TriZol protocol (Sigma) and diluted in water.

Cells were sorted by FACS from SEZ pooled from 10 adult hGFAP-eGFP animals. Following cell types were sorted as previously described (Fischer et al., 2011): quiescent adult neural stem cells (qNSC; hGFAP-GFP+, CD133+, EGFR-), activated adult NSC (aNSC; hGFAP-GFP+; CD133+, EGFR+) and ependymal cells (EC; hGFAP-GFP-, CD133+). In addition, in separate sorting using EGFR-APC, CD133-PE, and PSA-NCAM-PE, transiently amplifying progenitors (TAPs; EGFR+, CD133-, PSA-NCAM-) were identified. Also, staining for PSA-NCAM-PE and O4-APC allowed sorting of neuroblasts (NB; PSA-NCAM+, O4-). Finally, dissection of diencephalon from hGFAP-eGFP mice was used to sort diencephalon astrocytes (DA; hGFAP-GFP+). All antibodies used for FACS sorting will be specifically listed in the Key Resources Table. RNeasy Micro Kit (QIAGEN) was used to isolate total RNA according to manufacturer's manual. For both tissue and sorted cells, total RNA (200 ng) was re-transcribed into cDNA using Super Script III polymerase (Thermo Scientific Rockford, IL) with random primers and RNase Out (Thermo Scientific). qPCR reaction was performed using SYBR Green dye (Roche) in technical duplicates for each sample on a qPCR cycler (LightCycler 480 II, Roche) to determine relative expression of selected mRNA transcripts (denaturation for 10 min at 95°C, followed by 55 30 s cycles of 95°C denaturation and 60°C annealing and elongation). The results were analyzed using the LightCycler 480 Software (Roche) with the amplification cycle (Ct) values determined by maximum 2^{nd} derivation method and following the $2^{-\Delta\Delta Ct}$ method (Livak and Schmittgen, 2001) with normalization to the expression levels of GAPDH. The sequences of used primers (250 nM final concentration) were designed by using the Primer-BLAST online tool (NCBI-NIH): αENaC forward = CCCTCTGTCACGATGGTCAG, αENaC reverse = TCCGGAA CCTGTGCAGTAAC; βENaC forward = GCAGCTTCCTAAACAGCAGGTG, βENaC reverse = GCCGTGGGTGTTGGTGTTAT; γENaC forward = GCCAATCAGTGTGCAAGCAA; γENaC reverse = GGCCAGGTCAGTCTTGTTGA; GAPDH forward = TTCACCACCATGG AGAAGG; GAPDH reverse = CACACCCATCACAAACATGG.

A list of qPCR Primers and esiRNA can be found in Table S1.

BrdU and EdU Experiments

Animals were given BrdU (Sigma, 1 mg/ml) in drinking water (with 1% sucrose) for 14 days, followed by 7 days without BrdU. Then, the animals were given tamoxifen for 5 days as described above, followed by 7 days of EdU (Invitrogen, 0.2 mg/ml) in drinking water (with 1% sucrose). Animals were killed after the 7 days of EdU (meaning 7 days post treatment (DPT) and 19 days after BrdU). In the other paradigm, the animals were given Tamoxifen for 5 days as above and 3 days after that they received BrdU in drinking water and were killed 7 days after BrdU.

Immunohistochemistry

Animals were transcardially perfused with ice-cold PBS (40 ml) followed by perfusion with ice-cold 4% paraformaldehyde (PFA, 100 ml). The brains were isolated and postfixed in 4% PFA for 2-3 hours. The PFA was replaced by 30% sucrose and brains let to sink at room temperature. 40 μm sagittal sections (entire hemisphere containing SEZ) were cut in serial sets of 12 for stereological evaluation. Slide-mounted or free-floating immunohistochemistry (IHC) was performed. The en-face staining of whole-mount SEZ was based on a previously published protocol (Mirzadeh et al., 2010). The following primary antibodies were used: chicken polyclonal anti-green fluorescent protein (GFP; 1:400; Aves Labs Inc., Tigard, Oregon, USA); guinea-pig polyclonal anti-doublecortin (DCX; 1:300; Millipore-Merck, Darmstadt, Germany); rabbit polyclonal anti-Ki67 (1:200; Thermo Scientific Rockford, IL); rat monoclonal IgG2a,κ anti-Ki67 (1:300, eBioscience); rabbit monoclonal anti-phospho-p44/42 MAPK (Erk1/2) (1:400, Cell Signaling Technologies, Danvers, Massachusetts, USA), goat polyclonal anti-Sox2 (1:200; SC Biotechnology, Dallas, Texas, USA); mouse monoclonal IgG1 anti-glial fibrillary acidic protein (GFAP; 1:500; Sigma); mouse monoclonal IgG1 anti-S100β (1:200; Sigma); rabbit polyclonal anti-Olig2 (1:200; Millipore); rabbit polyclonal anti-cleaved caspase 3 (AC3; 1:100, Millipore); mouse anti-beta-Catenin (1:200; BD Biosciences, Heidelberg, Germany); rat polyclonal anti-BrdU (1:200; AbCam, Cambridge, UK). All secondary antibodies (1:300) were used as conjugated to respective fluorophores. For ENaC staining, rabbit anti-alpha-ENaC antibody (1:300, Stressmarq, Victoria, BC, Canada) was used followed by secondary anti-rabbit-Biotin conjugated antibody (1:300) and then streptavidin-HRP antibody (1:100, 1 hour at room temperature). The visualization utilized TSA-rhodamine (1:80, TSA System, Perkin Elmer, Waltham, MA, USA) for 8 minutes at room temperature.

Blocking with the carrier (1x PBS, 0.5% Tween 20, 5% normal goat serum) for 20 minutes at room temperature was followed by incubation with the primary antibodies at 4°C overnight. After 3 washes, the secondary antibodies were incubated for 1,5 hours at room temperature. Sections were counterstained with DAPI (1:1000; Roche). Slides were mounted and coverslipped using Aqua-Poly/Mount (Polysciences).

For BrdU staining, brain sections were incubated with primary antibodies for GFAP and GFP and followed by their respective antibodies as described above. After that, the sections were post-fixed in 4% PFA in PBS for 15 minutes in room temperature and treated with 0.3% citrate buffer (pH = 6) in a steamer cooker for 10 minutes. After cooling down the sections in PBS, primary antibody

for BrdU was applied overnight in 4°C, followed by 3 washes, and the secondary anti-rat fluorophore conjugated antibody. For EdU staining, sections were treated as described above and then subjected to the Click-iT EdU reaction (Invitrogen, Alexa Fluor A647 azide) according to the manufacturer's instructions.

For TUNEL staining, slide-mounted brain sections (tissue sampling fraction of 12) were pretreated with 85°C sodium citrate (0.1%, pH = 6.0, with 0.1% Triton X) for 5 minutes and stained for terminal deoxynucleotidyl transferase dUTP nick end labeling using the staining kit (Roche) according to the manufacturer's instructions to quantify TUNEL+ cells in SEZ.

Retroviral Cre delivery for Knock-out of ENaC in Fast Proliferating SEZ Cells *In Vivo*

To test the effects of alpha ENaC KO in fast proliferating cells *in vivo*, SEZ in both hemispheres of control (WT, n = 3) and iENaC KO (N = 4) mice were injected with retroviruses carrying cDNA of NLS-Cre recombinase under the CAG promoter (Colak et al., 2008). The NLS-Cre was cloned downstream of the CAG promoter in an expression vector based on previously published backbone (Tashiro et al., 2006) using the Gateway pENTR entry vector (Thermo Fisher) and the NLS-Cre sequence was confirmed by sequencing. The injections were performed using standard stereotaxic surgery approach with following coordinates (anterior-posterior: +0.7 mm relative to the bregma; medial-lateral: +/− 1.2 mm; dorsal-ventral: −1.9 mm). The animals were transcardially perfused 3 days after the injection and their brains cut in 40 μm thick sections sagittaly. All sections were stained for DAPI and the injection trace placement to SEZ was confirmed. Sections with GFP+ cells in SEZ were collected and stained for GFP, Ki67 and DCX as described above. The results are expressed as a proportion of GFP+Ki67+ cells and AC3+GFP+ out of total GFP+ cells.

Stereologic and Proportional Analyses

Quantification of GFP+ cells in SEZ was performed stereologically as described before (Petrik et al., 2012). All sagittal sections containing SEZ (in general, from +4.3 mm to +0.7 mm lateral to the midline) from two wells (separated by 6) in the series of 12 were stained for GFP and DAPI as described above. All GFP+ cells were quantified using a 25X objective on an epifluorescent microscope (Axio Observer Z1, Zeiss) by an observer blind to the genotype of the brains. The SEZ was defined as a band of tissue with densely packed cell somata, which aligned the lateral and anterior aspects of the lateral ventricle. Thickness of SEZ was measured on 2-3 confocal z stacks per animal. 3 measurements of maximal SEZ thickness were performed in each z stack using the manual linear measurement function in ImageJ. All thickness measurements per animal were averaged. For the olfactory bulb (OB), two different analyses were utilized. First, the total number of GFP+ cells was quantified stereologically as in SEZ in all sagittal sections (1 out of series of 6) containing the OB. Cells were counted in following anatomically defined layers: the glomerular, the external plexiform, the mitral and the internal plexiform layers. The cell counts from the mitral and internal plexiform layers were pooled. Second, for the granular layer with very high density of GFP+ cells, the number of GFP+ cells per cubic mm was estimated from two confocal z stacks scanned from tissue sections anatomically at 0.9-1.1 mm from the medial plane. The z stacks were precisely defined in all animals at the certain distance from the outer edge of the OB for the greatest reproducibility. The total number of GFP+ cells in SEZ and OB layers per hemisphere was thus expressed.

The proportional phenotyping analysis was performed as described previously. 3-4 sagittal sections containing SEZ and OB were stained for different markers as described above. In these sections, 2-3 randomized z stacks (optical sections of 2 μm) in SEZ or OB were scanned with 25X objective in a confocal microscope (LSM 710, Zeiss). The proportion of marker positive cells out of total GFP+ cells was obtained from phenotyping the cells from these scans using the Zen software (Zeiss). To obtain estimates of absolute number of marker-positive cells, the proportion of the marker-positive cells was multiplied by the strereologically obtained absolute counts of GFP+ cells as described previously (Petrik et al., 2012). In the case of rare marker-positive cells, such as AC3+ cells, the total number of cells was counted per entire SEZ without being expressed as double-positive with GFP (Petrik et al., 2013).

Electrophysiology

For *in situ* electrophysiology, acute coronal brain sections were prepared from Aldh1l1-GFP mice. The animals were anesthetized in isoflurane and decapitated. Brains were isolated into ice-cold cutting solution (containing in mM: 135 NMDG, 1.5 KCl, 1.5 KH_2PO_4, 23 choline-bicarbonate, 25 D-Glucose, 0.4 ascorbic acid, 0.5 $CaCl_2$, 3.5 $MgCl_2$; pH = 7.4, 310-330 mOsm) and cut on a VT1200 vibratome (200 μm thick; Leica, Wetzlar, Germany). The sections were collected to artificial cerebrospinal solution (ACSF, in mM: 125 NaCl, 3 KCl, 1.25 NaH_2PO_4, 25 $NaHCO_3$, 25 D-Glucose, 0.4 Ascorbic acid, 2 $CaCl_2$, 2 $MgCl_2$; pH = 7.4, 290-300 mOsm) oxygenated with 95% O_2/5% CO_2 and allowed to rest at 36°C for 1 hour, after which they were kept at room temperature. Sections were kept in the recording chamber in oxygenated ACSF with control constant flow (2 ml/min). The GFP+ cells with radial glia morphology in the SEZ were recorded in the whole-cell configuration (5-6 MΩ electrodes) with the following intracellular solution (in mM: 135 cesium methanesulphonate, 2 cesium chloride, 4 NaCl, 10 HEPES, 0.2 EGTA, 4 MgATP, 0.5 NaGTP, 10 phosphocreatine; pH = 7.3, 320-330 mOsm). Whole-cell recordings of identified cells were made in the voltage-clamp configuration with an EPC10-2 amplifier (HEKA Elektronik, Lambrecht, Germany). In the voltage-clamp mode, the passive membrane properties, such as resting membrane potential (RMP) and membrane resistance (IR) were monitored (with zero holding current) using the Patch Master software (HEKA Elektronik). Only the stable cells that did not change their RMP or IR by more than 5% during the entire recording protocol were used for further analysis. In the voltage-clamp mode, the cells were hyperpolarized from the RMP to −90 mV by a rectangular pulse (40 ms long). Cells were recorded every minute before (as control) and during perfusion with 50 μM Benz in ACSF in the recording chamber. When possible, also washout data were recorded using the same paradigm. Data were sampled at 10-30-μs intervals and low-pass filtered at 2 kHz using the EPC10 amplifier (HEKA). Recorded cells were photographed both in the brightfield and

the fluorescence using a CCD digital camera (Orca-D2, Hamamatsu, Herrsching, Germany). Using IGOR software (Wavementrics), Benz-sensitive currents (N = 3) were calculated as the difference between the resting current and steady-state hyperpolarized currents (at −90 mV) between control and after 6 minutes of Benz perfusion.

Shear Stress Experiments

The laminar shear stress of ACSF flow was calculated using the effective drag force equation (Althaus et al., 2007) for non-turbulent flow (with the drag coefficient, C_d, estimated to be around 1 for a surface perpendicular to the fluid flow but only 0.001 for a surface parallel to the flow, which is our case): $F_d = 0.5\theta A\omega^2 C_d$ (where F_d = the effective drag force, θ = density of water, A = effective surface, ω^2 = flow velocity). The effective shear forces are (F_{shear}) given by F_d/affected surface and are estimated to be 0.4 dyne/cm^2 for controls and for high flow conditions to be 2.0 dyne/cm^2, a value previously reported to increase the open probability of ENaC channels (Althaus et al., 2007). The velocity of the ACSF was measured to be about 3 cm.sec-1 with the tubing inner diameter of 1 mm being 1-2 mm from the SEZ whole-mount or the wall of the lateral ventricle in acute brain slices.

The shear stress experiments involved either acutely isolated brain sections (data not shown) or SEZ microdissected in the whole-mount preparation (Mirzadeh et al., 2010) from WT C57Bl6 or iENaC KO mice 10 DPT (N = 3 or more per group). The SEZ whole-mounts were subjected either to control (a whole-mount from the ipsilateral hemisphere) or elevated shear stress flow (from the contralateral hemisphere). The whole-mounts were allowed to rest for one hour after the microdissection in ACSF (oxygenated by 95% O_2/5% CO_2) on a mesh in a beaker, then anchored *en face* to the bottom a perfusion chamber by a standard wire mesh patch-clamp anchor, or kept in the beaker (for controls). The whole-mounts were subjected for 4 hours to the ACSF pumped by a peristaltic pump (Minipuls 3, Gilson, Middleton, WI, USA) and out-flowing from tubing to the whole-mount in the caudal to rostral direction. After this, the whole-mounts were fixed in 4% PFA overnight and stained for Ki67, DCX, GFP and DAPI as described above. In total, 3-5 systematic random confocal z stacks were scanned per a whole-mount from the surface of the lateral ventricle to 40 μm depth and used for estimating either the number of Ki67+ and Ki67+DCX+ cells or number of phospho-Erk+Ki67+ and pErk+Ki67+ DCX+ cells per mm^3 (in WT mice) or the proportion of Ki67+GFP+/GFP+ and Ki67+DCX+GFP+/GFP+ cells (in iENaC control and KO mice). In addition, a different set of SEZ whole-mounts (with corresponding controls) from WT C57Bl6 mice was subjected for 4 hours to the elevated shear stress with ACSF containing Benzamil (10 μM) or BTP-2 (YM-58483, Selleckchem, 1 μM from a 10 mM stock in DMSO).

Sodium Imaging

Acute brain sections (250 μm) from adult iENaC KO and control mice (21 DPT) were prepared as described above. After 30 minutes of rest at 37°C, a slice was anchored in the recording chamber by a custom-made platinum grid with the SEZ being 2-3 mm to the opening of the perfusion tubing. Cells in SEZ were bolus-loaded with the membrane-permeable sodium indicator SBFI-AM (Thermo, 250 μM final concentration in 1x PBS from 1 mM stock diluted in DMSO with 20% pluronic acid) using a glass pipette as described earlier (Meier et al., 2006). SEZ was repeatedly (usually 10 times) injected with 7-10 s pulses of 1.5 psi (0.1 bars, 10 kPa). After an additional 30 minute room temperature incubation to allow for the deesterification of SBFI-AM, the SEZ was searched for GFP+ cells that were loaded with SBFI-AM. Fluorescence was recorded at room temperature using wide-field fluorescence imaging. Specifically, we used a variable scan digital imaging system (Nikon NIS-Elements v4.3, Nikon GmbH Europe, Düsseldorf, Germany) attached to an upright microscope (Nikon Eclipse Fn-PT, Nikon GmbH Europe, Düsseldorf, Germany) and an ORCA FLASH V2 camera (Hamamatsu photonics Deutschland GmbH, Herrsching, Germany). Images were collected with a LUMPlanFL 40 × objective (water immersion, N.A. 0.8, Olympus Europe, Hamburg, Germany). Ratiometric sodium imaging was performed by alternating excitation of SBFI at 340 nm (weakly sodium-sensitive wavelength) and 380 nm (sodium-sensitive wavelength) with sampling frequency of 1 Hz. SBFI emission (> 440 nm) was collected in defined regions of interest (ROI) representing cell bodies, located at the interface between SEZ and ACSF. For the perfusion protocol, the brain slice was subjected to 1-2 minutes of baseline flow followed by 2-3 minutes of high flow and back to control flow. Standard dynamic background correction was performed as described earlier (Langer and Rose, 2009). After background correction, the fluorescence ratio (F_{340}/F_{380}) was calculated for the individual ROIs and analyzed offline using OriginPro 9G Software (OriginLab Corporation, Northhampton, MA). Recorded imaging videos with corresponding ROIs were inspected for movement artifacts and to ensure the proper ROI placement. ROIs were grouped into two classes based on their responsiveness to the high flow (non-responding and positively responding). For the fluorescence amplitude measurements, the fluorescence was averaged for the data points during the last 20-30 s of the baseline flow and during the 20-30 s of the high flow plateau fluorescence. The results are expressed as percent change over baseline in the fluorescence ratio. From a previous *in situ* calibration of SBFI, performed as described in detail elsewhere (Meier et al., 2006), we estimated that 1% of SBFI normalized ratio fluorescence corresponds to about 1.1 mM change in intracellular sodium concentration.

Calcium Imaging

Acute brain sections from adult iENaC KO and control mice (10 DPT) were prepared as described above, and a calcium indicator was loaded into cells by a loading protocol modified from a previous study (Lacar et al., 2010). One hour after cutting, individual coronal sections containing the lateral ventricle cross-section were placed in a 24-well plate with 600 μL of ACSF containing Oregon Green 488 Bapta-1, AM (OGB-1, Life Technologies) in final concentration of 40 μM, diluted from a freshly prepared 4 mM OGB-1 stock solution of 50 μg of OGB-1 dissolved in 20 μL of DMSO (with 20% pluronic acid, Sigma). Sections were incubated at 35°C (95% O_2/5% CO_2 atmosphere) for 30 minutes, washed twice in ACSF and placed in the recording chamber (with constant ACSF perfusion bubbled

with 95% O_2/5% CO_2) on a poly-L-lysine-coated coverslip anchored by a custom-made platinum grid. The opening of the perfusion tubing was placed as described above, only a few millimeters from the brain section with the dorsal edge facing the tube opening. Cells in the SEZ with loaded OGB-1 were imaged at room temperature by a 16X, 0.8 NA water immersion objective (Nikon) on an Acera 2-photon microscope (Thorlabs), equipped with an 8 kHz resonant scanner and driven by a MaiTai eHP DS tunable Ti:Sapphire laser (Spectra-Physics). OGB-1 was excited at 775 nm with an average power of 40-50 mW at the specimen plane. Frame scans of 512 × 512 pixels were acquired at 30 Hz with an imaging area of ~200 × 200 μm using ScanImage (Pologruto et al., 2003). The SEZ of the brain section was subjected to the following perfusion paradigm during the uninterrupted imaging: 15 minutes of baseline low-flow rate (F_{shear} estimated to be 0.4 dyne/cm^2) followed by 15 minutes of high-flow rate of elevated shear-stress (F_{shear} estimated to be 2.0 dyne/cm^2) and followed by an additional 15-30 minutes of recovery with low-flow rate identical to baseline. After the calcium imaging paradigm, z stacks of the recorded area were taken for OGB-1 (at 775 nm) and for GFP (at 930 nm) for post hoc identification of GFP-positive OGB-1-loaded cells. The large separation in 2-photon excitation cross-section between OGB-1 and GFP allowed near perfect isolation of fluorescence, even though the molecules have similar emission spectra. 3-4 sections per animal were used, and each section was subjected to the perfusion paradigm only once. The post hoc analysis was performed using custom-written routines in MATLAB (Mathworks). First, image sequences were registered for movement artifacts using a discrete Fourier transform algorithm and thereafter averaged for every 40 frames to obtain a final frame-rate of 0.75 Hz. Then regions of interests (ROIs) were manually traced around OGB-1-loaded cells. ROIs were classified for GFP expression (based on overlap of the dual-wavelength z stacks) and putative cell type (based on rough morphology and position in the SEZ). For the latter, the following classes were visually discriminated: adult neural stem cells (NSCs, radial glia-like morphology, in SEZ relatively close but not within to the ependymal layer), transiently amplifying progenitors (Progenitors, larger soma, no obvious processes, within SEZ), neuroblasts (NB, eye-shaped bipolar soma, usually with two short processes and usually entering the RMS), and ependymal cells (any cells directly in the ependymal layer). For each ROI the time-series of the entire imaging session was then analyzed with a semi-automated event detection algorithm. Here, the average intensity of the ROI was baseline-normalized (background fluorescence was not subtracted) and further low-pass filtered at 0.15 Hz with a Gaussian smoothing algorithm. Calcium events were then identified from peaks in the first derivative of fluorescence changes (ΔF/F), based on a threshold that was manually set (0.006-.02) for each ROI to accommodate differences in event shape and signal-to-noise ratio between ROIs. ROIs were triaged when events could not be consistently detected throughout the entire imaging session (i.e., if the baseline was not stable or the signal was too noisy). This method of detection therefore predominantly identified slow, robust calcium events lasting on average 10-15 s. Faster calcium events with smaller amplitudes were not included in the analysis because their detection was generally unreliable due to fluorescence baseline noise. All the analyzed, stable ROIs were further annotated into the following three groups by their overall responsiveness to the high-flow compared to the baseline: positive responders (that had a higher frequency of calcium events during high-flow than during baseline), non-responders (that had the same frequency of calcium events during high-flow and baseline) and negative responders (that had a lower frequency of calcium events during high-flow than during baseline).

SEZ whole-mounts were dissected from WT C57bl6 mice as described above. After dissection, the whole-mounts were rested for 30 minutes in ACSF oxygenated with Carbogen before incubated in 40 μM OGB-1 as described for the acute brain sections. After incubation, the whole-mount was mounted on PDL-coated coverslip with the ventricular surface facing up and anchored in the recording chamber as described above. To visually detect the surface, the ACSF was supplemented with Alexa 594 (1:10.000). Calcium imaging was performed in a z stack consisting of 10 focal planes (512 × 512 pixels) separated by 3 μm that was taken continuously with 3 Hz frequency. Each ROI was followed by a MATLAB custom-written automated detection system, which allowed an online-analysis of the fluorescence changes in the 3-D tracked ROI volume. The whole-mounts were subjected to the same perfusion paradigm as the acute slices. The stem/progenitor cells were identified by their morphology and separated into two groups. The surface cells were at the contact with the ventricle within the top 10 μm from the tissue interface. The deep cells were located in SEZ depths from about 10 to 30 μm. Each ROI was visually inspected post hoc for containing calcium events and relatively stable baseline. The analysis of fluorescence changes was done as described for the acute brain sections.

STATISTICAL ANALYSIS

Numbers of biological and technical repeats are provided in the Figure Legends and in the Method Details. Datasets were analyzed with Microsoft Excel and GraphPad Prism 6. Non-parametric statistical tests (Mann-Whitney for un-paired experiments, Wilcoxon matched-pairs signed rank test for paired experiments) were used in all experiments but in the following. Mann-Whitney test was used in all cases but the following figure panels, when Wilcoxon test for paired experiments was used: Figures 2N and 5D. Parametric tests were used in the case of proven normal distribution (tested by D'Agostino & Pearson's omnibus normality test) or when the use of non-parametric tests is prohibitive, meaning in cases where n = 3. The T-Test with proven normal distribution was used in the following figure panels: Figures 2K, 6I, 6J, S2I and S6H. The contingency distribution of data were analyzed either by either Chi-square or Fisher's exact tests as in Figures 6H and S6G. Results were considered significant with $p < 0.05$ (one asterisk). In graphs, two asterisks represent values of $p < 0.01$, three asterisks for $p < 0.001$. Results are presented as mean ± standard error of mean (SEM) in the datasets with proven normal distribution. In all other cases, results are presented as median ± interquartile range (IQR), which better represents datasets tested by non parametric tests (that compare medians) or datasets with smaller N. The

representation of the data is annotated in the figure legends. The IQR was calculated as R = P * (n + 1)/100, where P is the desired percentile (25 or 75 for quartiles) and n is the number of values in the dataset (Hyndman and Fan, 1996). The result is the rank that corresponds to the percentile value.

DATA AND SOFTWARE AVAILABILITY

The raw data have been uploaded to Mendeley at https://doi.org/10.17632/kp7v8mkf3s.2 and https://doi.org/10.17632/8brx3kx9ky.2. Download links for software used in this study are provided in the Key Resources Table.